J. Mech. Phys. Solids 160 (2022) 104759

Contents lists available at ScienceDirect

Journal of the Mechanics and Physics of Solids

journal homepage: www.elsevier.com/locate/jmps

Particle size effects in ductile composites: An FFT homogenization study

M. Magri [a,*], L. Adam [b], J. Segurado [c,a,**]

[a] IMDEA Materials Institute, C/ Eric Kandel 2, 28906, Getafe, Madrid, Spain
[b] e-Xstream Engineering, Axis Park-Building H, Rue Emile Francqui 9, B-1435 Mont-Saint-Guibert, Belgium
[c] Departamento de Ciencia de Materiales, E. T. S. de Ingenieros de Caminos, Universidad Politécnica de Madrid, Calle Profesor Aranguren 3, 28040 Madrid, Spain

ARTICLE INFO

Keywords:
Strain gradient plasticity
Ductile damage
Particle reinforced composites
Implicit gradient regularization
FFT homogenization

ABSTRACT

We present a computational homogenization study on the particle size effect in ductile composites. The micromechanical formulation is based on non-local models through (i) the incorporation of a lower-order strain gradient plasticity model and (ii) the application of an implicit gradient regularization technique to the Gurson–Tvergaard–Needleman ductile damage model for metals. In this way, the extended model is equipped with two length-scale parameters, one for each non-local extension, which modulate the size dependent character of the formulation. The problem consists of a system of partial differential equations in which two Helmholtz-type equations for the damage regularization are coupled with the balance of linear momentum through the stress, which depends on the non-local variables and on the plastic strain gradient.

A series of numerical simulations are conducted to investigate the behavior of three-dimensional microstructures representative of particle reinforced metal matrix composites. The change in strengthening and ductility, as a function of the particle size, is first analyzed by means of a parametric study in which the considered non-local extensions act both independently and together. Finally a comparative study with experimental results demonstrates that the particle size induced strengthening in metal matrix composites can be quantitatively captured by the considered model.

1. Introduction

Particle reinforced metal matrix composites consist of a metal matrix whose stiffness and strength is enhanced by the addition of hard reinforcing particles, resulting in advanced materials commonly used in the automotive and aerospace industries (Ibrahim et al., 1991). In such composite structures, the mechanisms controlling the overall strength and ductility typically operate at different length scales since heterogeneities of different size characterize their material microstructure (Babout et al., 2001, 2004; Weck et al., 2008). In particular, the overall mechanical response of particle reinforced metal matrix composites shows a prominent size effect connected to the size of the reinforcing particles (Lloyd, 1994; Gustafson et al., 1997; Dai et al., 2001; Milan and Bowen, 2004; Liu et al., 2014). For instance, at a constant particle volume fraction it has been observed an increase in strength with decreasing

* Corresponding author.
** Corresponding author at: Departamento de Ciencia de Materiales, E. T. S. de Ingenieros de Caminos, Universidad Politécnica de Madrid, Calle Profesor Aranguren 3, 28040 Madrid, Spain.
E-mail addresses: marco.magri@imdea.org (M. Magri), javier.segurado@imdea.org (J. Segurado).

https://doi.org/10.1016/j.jmps.2021.104759
Received 5 July 2021; Received in revised form 30 November 2021; Accepted 18 December 2021
Available online 12 January 2022

particle size. In addition to that, the size of the particles influences the ductility of the composite material, although in this case bigger particles can increase or decrease the ductility depending on the dominant damage mechanism (Lloyd, 1994).

Different factors contribute to these prominent size effects such as the distribution of the particles, the local stress triaxiality as well as the mechanical properties of both metal matrix and reinforcements. As a result, the size dependence of the mechanical response in particle reinforced metal matrix composites is particularly complex and a quantitative understanding is still lacking.

The rise of computational power, parallelization methods, and the development of more efficient solvers have increased the potential of micromechanics based predictive models that, in conjunction with experiments, can speed-up significantly the design of advanced materials with complex microstructures (Matouš et al., 2017). In computational micromechanics, the mechanical behavior of composite materials is predicted at a microscopic scale within a suitable Representative Volume Element (RVE), i.e. a statistically representative digital description of the material microstructure. In the context of metal matrix composites, numerous studies have analyzed the impact of the composite microstructure on the mechanical response either by considering different failure mechanisms separately – e.g. ductile failure in the matrix material (LLorca and Segurado, 2004), debonding (Segurado and LLorca, 2005), and particle fracture (Böhm et al., 2004) – or by accounting for the combination of multiple damaging processes (Huber et al., 2005; Shakoor et al., 2018; Dorhmi et al., 2020). Nevertheless, such models rely on conventional local mechanics, so the influence of size on the plastic-damage processes cannot be accounted as the relevant governing equations are insensitive to dimensional changes. In addition, the simulation of damage in continuum mechanics gives rise to a well-known pathological grid dependence of the numerical solution, thus limiting the validity of the results to the adopted level of the spatial discretization of the RVE (Jirasek, 2007).

The characteristic size dependence of plastically deformed metals at micron and submicron scales can be effectively captured by the so-called Strain Gradient Plasticity (SGP) models (Aifantis, 1987; Voyiadjis and Song, 2019). Despite the lack of a unified general theory, such formulations are generally categorized in the following two distinct groups: (i) *higher-order* SGP (Fleck et al., 1994; Fleck and Hutchinson, 2001; Gurtin and Anand, 2005; Gudmundson, 2004) and (ii) *lower-order* SGP models (Bassani, 2001; Nix and Gao, 1998). In the former class, strain gradients are included in the description of the continuum kinematics so that, according to the *principle of virtual work*, an additional microforce balance equation, involving higher order stresses, is coupled with the classical balance of linear momentum. On the other hand, lower-order strain gradient theories include the effect of strain gradients only at the constitutive level by prescribing strain gradient dependent hardening moduli. The main benefit of this second approach is that the structure of conventional continuum mechanics is preserved and, therefore, classical numerical algorithms, such as traditional Finite Elements (FE), can be still employed with little modifications. In both cases, the model includes a length scale parameter which controls the influence of the plastic strain gradient in the material response.

When damage and fracture of ductile metals are considered, an additional size dependence of the problem is related to the absolute size of the region in which microscopic damage mechanisms take place. The use of classical continuum damage mechanics for modeling this process typically leads to the loss of ellipticity of the relevant governing equations. As a consequence, their numerical solution produces non-objective results since damage localizes in a band whose size depends on the discretization level (Eringen, 1966). The regularization of such a damage localization through non-local models suppresses this problem by introducing a length parameter that controls damage localization and, therefore, rules the size effect when modeling damage. Among different non-local theories (Jirasek, 2007), the so-called *implicit gradient regularization* enhances the constitutive equations through some non-local fields, typically a scalar measure of the plastic strain, which are the solution of additional partial differential equations (Peerlings et al., 1996). In this way, the resulting formulation is an enriched problem where the classical balance of linear momentum is fully coupled with a Helmholtz-type equation for each of the non-local variables. The numerical implementation of this coupled problem is, therefore, much more expensive than the one of classical damage mechanics and the simulation of regularized damage models in complex multi-phase microstructures is nowadays limited by the use of traditional FE solvers.

As a result of the aforementioned limitations involved with the implementation of SGP formulations and non-local damage models, only a few numerical works have studied the effect of particle size on the strengthening and ductility in metal matrix composites. For example, the strengthening size effect was analyzed via the implementation of a lower-order SGP model in two-dimensional (Yan et al., 2007; Zhou et al., 2011) and three-dimensional (Zhang et al., 2019) microstructures using FE. The influence of damaging processes was also considered in order to study the particle size effect on both ductility and strengthening in Weng et al. (2019) and Ban et al. (2020). In particular, Weng et al. (2019) presented three-dimensional simulations accounting for particle size effects in the strength through the use of a lower-order SGP model coupled with interface damage. Similarly, Ban et al. (2020) studied the coupled size effects of plasticity and damage by means of idealized single-particle axisymmetric simulations including particle–matrix debonding and ductile failure in the matrix material. This last model combines size effects in strengthening and ductility by making the intrinsic length scale of the adopted SGP formulation as a function of damage evolution. However, the model still relies on a classical (local) version of the Lemaitre damage model (Lemaitre, 1985). In general, the use of non-local damage mechanics in micromechanical simulations of particle reinforced composites is very limited because of some intrinsic difficulties, e.g. the extension of existing non-local formulations to heterogeneous media and the high computational cost of the resulting models. Therefore, the available numerical studies employ simple damage models (Drabek and Böhm, 2006, 2005) or are restricted to two-dimensional setting (Reusch et al., 2008). Only recently, the numerical implementation of regularized damage models in heterogeneous media via solvers based on Fast-Fourier-Transforms (FFT) has shown promising perspectives for the simulation of non-local problems with complex microstructures (Magri et al., 2021).

In this work, we present a numerical study on the size dependent mechanical response of particle reinforced metal matrix composites in the field of computational homogenization. As discussed in Section 2, to account for size effects, the damage model for microvoid nucleation, growth, and coalescence of Tvergaard and Needleman (1984) is purposely extended via (i) the incorporation

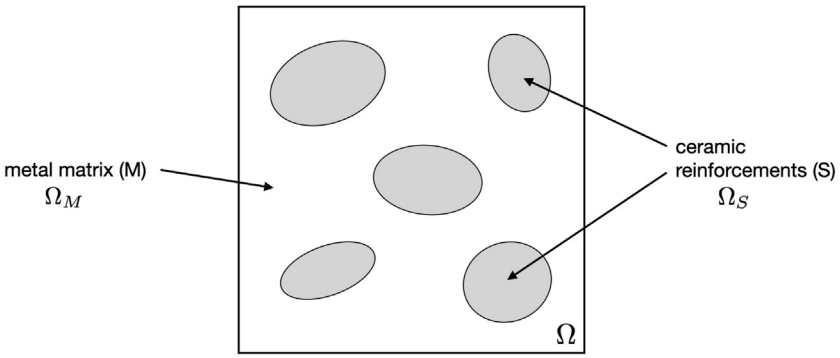

Fig. 1. Schematic of the microscopic arrangement of a particle reinforced metal matrix composite.

of the lower-order SGP model of Huang et al. (2000) and (ii) the application of the implicit non-local damage regularization for heterogeneous materials derived in Magri et al. (2021). For simplicity, alternative damaging mechanisms, e.g. particle–matrix debonding or particle fracture, are not included here. The resulting formulation is a non-conventional mechanical problem consisting of three coupled partial differential equations. This problem is numerically solved via the iterative staggered algorithm described in Section 3 that exploits the sequential usage of FFT-Galerkin and conjugate gradient based solvers. The impact of the non-local extensions on the composite mechanical response is analyzed in Section 4 through a series of parametric studies. Finally, a comparison with experimental results demonstrates the capability of the present formulation of capturing quantitatively the typical particle size dependent strengthening in metal matrix composites.

2. Model description

A metal matrix composite is here idealized as a biphasic medium consisting of ceramic reinforcements embedded in a metallic matrix, as represented schematically in Fig. 1. The RVE, with volume Ω, is then characterized by the presence of a reinforcing material (denoted by S), which occupies an overall volume Ω_S, and a matrix material (denoted with M) with volume Ω_M. The condition $\Omega = \Omega_M \cup \Omega_S$ thus holds. Mechanical equilibrium is prescribed by the local form of the balance of linear momentum in the absence of inertial and body forces

$$\mathrm{div}[\boldsymbol{\sigma}] = \vec{0}\,, \tag{1}$$

where $\boldsymbol{\sigma}$ is the Cauchy stress tensor.

The reinforcements are assumed to behave as elastic solids insensitive to damage. Their mechanical behavior corresponds to the one of an elastic isotropic solid with Young modulus E_S and Poisson coefficient ν_S. On the other hand, the material model of the metallic matrix incorporates the physical processes that characterize ductile fracture of metals, namely void nucleation, growth, and coalescence. In this regard, we select the phenomenological extension proposed by Tvergaard and Needleman (1984) (known as the GTN model) of the physically-based model for void growth of Gurson (1977). Two extensions of the classical version of the GTN model are introduced here. Firstly, to deal with a well-posed failure model, a non-local regularization of the GTN model will be considered. Secondly, a lower-order strain gradient plasticity model will be incorporated in the evolution of the flow stress to capture the size dependent strengthening induced by the reinforcing particles.

2.1. The GTN model

The classical version of the GTN model is characterized by the definition of the so-called effective porosity f_*, which quantifies the level of damage induced by the presence of voids in the material matrix. The mechanical degradation related to the presence of porosity is taken into account by the definition of the following yield surface

$$\phi(\sigma, \epsilon_0^p,\, f_*) = \left(\frac{s}{\sigma_{flow}}\right)^2 + 2\, f_*\, q_1 \cosh\left(-\frac{3}{2}\frac{q_2\, p}{\sigma_{flow}}\right) - \left(1 + q_1^2\, f_*^2\right)\,, \tag{2}$$

where ϵ_0^p is the matrix equivalent plastic strain and σ_{flow} the matrix flow stress. The parameters q_1, q_2 are phenomenological adjusting coefficients, while s and p refer to the Mises equivalent stress and hydrostatic pressure, respectively, i.e.

$$s = \sqrt{\frac{3}{2}\,\boldsymbol{s} : \boldsymbol{s}} \quad \text{and} \quad p = -\frac{1}{3}\mathrm{tr}\,[\boldsymbol{\sigma}]\,,$$

being $\boldsymbol{s} = \mathrm{dev}\,[\boldsymbol{\sigma}]$ the deviatoric stress tensor. Eq. (2) implies that the plastic behavior is pressure dependent for non-zero values of the effective porosity. The latter affects the yield surface by decreasing the set of admissible stress states as f_* increases, leading

eventually to a complete loss of bearing capacity of the material matrix. This condition is reached for a limit value of the effective porosity f_V^* that can be calculated by imposing $\phi = 0$ at zero stress, namely

$$f_V^* = \frac{1}{q_1} .$$

The stress tensor $\boldsymbol{\sigma}$ is defined according to an isotropic linear elastic law in rate form

$$\dot{\boldsymbol{\sigma}} = K \, \mathrm{tr} \left[\dot{\boldsymbol{\varepsilon}} - \dot{\boldsymbol{\varepsilon}}^p \right] \boldsymbol{I} + 2 \mu \, \mathrm{dev} \left[\dot{\boldsymbol{\varepsilon}} - \dot{\boldsymbol{\varepsilon}}^p \right] , \tag{3}$$

where K and μ are the bulk and shear moduli. Symbols $\boldsymbol{\varepsilon}$ and $\boldsymbol{\varepsilon}^p$ refer to the total and plastic strains, while a superposed dot indicates a partial time (or more precisely *pseudo*-time) derivative. In the realm of small strain analysis, a standard additive decomposition of the rate of strain tensor of type

$$\dot{\boldsymbol{\varepsilon}} = \dot{\boldsymbol{\varepsilon}}^e + \dot{\boldsymbol{\varepsilon}}^p$$

is adopted, where $\boldsymbol{\varepsilon}^e$ is the elastic strain. The evolution of the plastic strain tensor $\boldsymbol{\varepsilon}^p$ is derived from application of the *normality rule*

$$\dot{\boldsymbol{\varepsilon}}^p = \lambda \frac{\partial \phi}{\partial \boldsymbol{\sigma}} = \lambda \left[\frac{\partial \phi}{\partial p} \frac{\partial p}{\partial \boldsymbol{\sigma}} + \frac{\partial \phi}{\partial s} \frac{\partial s}{\partial \boldsymbol{\sigma}} \right] , \tag{4}$$

where λ identifies the plastic multiplier. In standard rate independent plasticity (Simo and Hughes, 2006), the plastic multiplier is calculated by exploiting the so-called *persistency condition*, i.e. by imposing $\dot{\phi} = 0$ if $\lambda > 0$. The inelastic material behavior is then completed by the evolution of the internal variables ϵ_0^p and f_*. In the GTN model, the evolution of the matrix equivalent plastic strain reads[1]

$$\dot{\epsilon}_0^p = \frac{\boldsymbol{\sigma} : \dot{\boldsymbol{\varepsilon}}^p}{(1-f) \, \sigma_{flow}} , \tag{5}$$

where f is the actual void volume fraction defined in the spirit of Gurson (1977). The constitutive definition of the matrix flow stress σ_{flow} will be discussed in Section 2.3 along with the incorporation of strain gradient effects. The kinetics of evolution of the effective porosity f_* is established to model the physical processes taking place in ductile fracture of metals, namely (i) void nucleation, (ii) void growth, and ultimately (iii) formation of macro cracks due to void coalescence. The latter process is prescribed using the following phenomenological law

$$f_*(f) = \begin{cases} f & \text{if} \quad f < f_C , \\ f_C + \dfrac{f_V^* - f_C}{f_F - f_C} (f - f_C) & \text{if} \quad f_C \le f < f_F , \\ f_V^* & \text{if} \quad f \ge f_F , \end{cases} \tag{6}$$

where f_C is a critical void volume fraction above which void coalescence activates, while f_F refers to the void volume fraction at fracture. Finally, the evolution of f reads

$$\dot{f} = \dot{f}_{nucl} + \dot{f}_{growth} , \tag{7}$$

being $\dot{f}_{nucl}$ and $\dot{f}_{growth}$ the time variation of the porosity due to the mechanisms of void nucleation and growth, respectively. According to Nguyen et al. (2020), these functions have to be properly defined in order to deal with an objective formulation of ductile failure. Such aspects will be summarized next.

2.2. Non-local regularization of the GTN model

A suitable regularization of the GTN model requires the kinetics of nucleation and growth processes to be established in terms of non-local plastic variables, as follows

$$\dot{f}_{nucl} = \mathcal{A}_N \left(\overline{\epsilon_0^p} \right) \dot{\overline{\epsilon_0^p}} , \qquad \text{and} \qquad \dot{f}_{growth} = (1-f) \, \dot{\overline{\epsilon_V^p}} ,$$

where $\mathcal{A}_N$ is a strain rate controlled nucleation rate, while $\overline{\epsilon_0^p}$ and $\overline{\epsilon_V^p}$ are the non-local counterparts of the matrix equivalent plastic strain and the volumetric part of the plastic strain in the porous material, ϵ_0^p and $\epsilon_V^p = \mathrm{tr}[\boldsymbol{\varepsilon}^p]$ respectively. According to Chu and Needleman (1980), the void nucleation function reads

$$\mathcal{A}_N \left(\overline{\epsilon_0^p} \right) = \frac{f_N}{s_N \sqrt{2\pi}} \exp \left[-\frac{1}{2} \left(\frac{\overline{\epsilon_0^p} - \epsilon_N}{s_N} \right)^2 \right] . \tag{8}$$

[1] For the sake of clarity, it is remarked that symbol $\boldsymbol{\varepsilon}^p$ identifies the plastic strain tensor in the porous metal while the slightly different symbol ϵ_0^p refer to the scalar matrix equivalent strain.

where in Eq. (8), f_N, ϵ_N and s_N are material parameters. f_N represents the volume fraction of void nucleating particles while ϵ_N and s_N correspond to the mean value and standard deviation of the strain necessary to nucleate a void. Note that the classical specifications of $\dot{f}_{nucl}$ and $\dot{f}_{growth}$, as given in Tvergaard and Needleman (1984), can be recovered by replacing the non-local variables with their local counterparts. The introduction of the non-local variables in the evolution of damage is employed in order to avoid strain localization during fracture propagation.

The definition of the non-local variables $\overline{\epsilon^p}$ and $\overline{\epsilon^p_V}$ depends on the particular type of regularization employed. In this work, an implicit gradient approach has been chosen because it results in additional partial differential equations which allow the formulation of the regularized problem with local equations. Moreover, due to the form of the additional field equations, the implicit gradient model is particularly suitable for the numerical solution through FFT-based algorithms, as shown by Magri et al. (2021), whose formulation will be followed here.

In the implicit gradient regularization, the non-local plastic strain variables are solutions of the following partial differential equations of Helmholtz type

$$\overline{\epsilon^p_0} - \operatorname{div}\left[\ell_d^2\,(\vec{x})\ \nabla\overline{\epsilon^p_0}\right] = \epsilon^p_0\,, \tag{9a}$$

$$\overline{\epsilon^p_V} - \operatorname{div}\left[\ell_d^2\,(\vec{x})\ \nabla\overline{\epsilon^p_V}\right] = \epsilon^p_V\,, \tag{9b}$$

where ℓ_d is a material parameter with the unit of length that introduces an internal length scale related to the damage process. From a strictly mathematical point of view, ℓ_d can be treated exclusively as a parameter related to the non-local regularization of damage (i.e. to state a well-posed boundary value problem). To produce an effective non-local regularization, the magnitude of ℓ_d has to be selected at least as the size of a couple of voxels. Nevertheless, ℓ_d might be connected to the physical mechanisms underlying ductile fracture. More specifically, ℓ_d can be interpreted in terms of the average distance between micro-voids in the materials, i.e. the one that are described in a homogenized sense – or the size of a process zone – i.e. the thickness of the damage bands. Following this path of reasoning, ℓ_d shall not be treated as an intrinsic material parameter, but rather identified based on the specific material microstructure and on the scale at which the material is idealized (e.g. the size of microvoids is much smaller than the reinforcing particles). Therefore, for the scope of this study, it seems legitimate to select ℓ_d with the same order magnitude of the reinforcing particles since the thickness of the fracture zone is expected to be of that size.

In the context of FFT-based solvers, the non-local averaging equations are resolved in the whole domain Ω and, although the source of $\overline{\epsilon^p}$ and $\overline{\epsilon^p_V}$ are restricted to the matrix, the resulting non-local fields can enter the regions occupied by the elastic reinforcements Ω_S. Moreover, the parameter ℓ_d has to be assigned to the elastic phases as well. As proven in Magri et al. (2021), if ℓ_d is specified as

$$\ell_d\,(\vec{x}) = \begin{cases} \ell_d^M & \text{if} \quad \vec{x} \in \Omega_M\,, \\ \ell_d^S & \text{otherwise}\,, \end{cases} \tag{10}$$

with $\ell_d^S/\ell_d^M \to 0$, a free-Neumann interface condition between reinforcing particles and metal matrix is recovered. In fact, setting $\ell_d^S/\ell_d^M \ll 1$ prevents spurious diffusion of non-local variables, and thus the propagation of fracture, from the damageable matrix to the elastic phases.

2.3. Mechanism-based strain gradient plasticity

In order to study particle size-effects in metal matrix composites, the GTN model is extended to include the effects of strain gradients in the work hardening law. Due to its simplicity and physical background, we selected the so-called mechanism-based strain gradient plasticity model (MSGP) developed by Nix, Gao, Huang and co-workers (Nix and Gao, 1998; Gao et al., 1999; Huang et al., 2000, 2004). Unlike other strain gradient theories of phenomenological nature, the MSGP introduces plastic strain gradients in the work hardening law based on microscopic dislocation mechanisms via the notion of *geometrically necessary dislocations* (GNDs). Since the effect of the strain gradients is introduced only at the constitutive level, the thermodynamic consistency of the model is satisfied without the introduction of higher order stresses. This model falls in the class of the so-called lower-order strain gradient plasticity models as the conventional structure of continuum mechanics is preserved. As a consequence, no additional boundary conditions need to be set to prescribe flux of dislocations through the boundaries (e.g. micro-hard or micro-free conditions) and plastic strain gradients develop naturally.

The starting point of the MSGP is the crystal level, where the model assumes that the critical resolved shear stress for plastic flow in a slip system, τ_{flow}, is a function of the dislocation density, following the Taylor model (Taylor, 1934, 1938)

$$\tau_{flow} = \beta\,\mu\,b\,\sqrt{\rho_S + \rho_G}\,, \tag{11}$$

where $\beta \simeq 0.3$ is an empirical coefficient, μ the shear modulus, b the magnitude of Burgers vector, while symbols ρ_S and ρ_G denote the densities of *statistically stored dislocations* (SSDs) and GNDs, respectively. According to Nye (1953) and Ashby (1970), the density of geometrically necessary dislocations is linked to a suitable scalar measure of the plastic strain gradients, η^p, as follows

$$\rho_G = \bar{r}\,\frac{\eta^p}{b}\,, \tag{12}$$

being $\bar{r} \simeq 1.9$ the so-called Nye factor defined in Arsenlis and Parks (1999). The macroscopic tensile flow stress of a polycrystal, σ_{flow}, is then proportional to τ_{flow} through the Taylor factor $M \simeq 3.06$, namely

$$\sigma_{flow} = M\,\tau_{flow}\,,$$

which, substituted into Eq. (11) and in view of Eq. (12), gives

$$\sigma_{flow} = M\,\beta\,\mu\,b\,\sqrt{\rho_S + \bar{r}\frac{\eta^p}{b}}\,. \tag{13}$$

In the particular case of uniaxial tension, the plastic strain is uniform and the plastic strain gradients vanish. Accordingly, σ_{flow} is equivalent to the conventional flow stress σ_0, namely

$$\sigma_0 = M\,\beta\,\mu\,b\,\sqrt{\rho_S}\,, \tag{14}$$

so that the density of SSDs can be simply estimated as function of σ_0 as

$$\rho_S = \left(\frac{\sigma_0}{M\,\beta\,\mu\,b}\right)^2\,. \tag{15}$$

In a general scenario, the conventional flow stress is expressed in terms of the equivalent plastic strain ϵ^p as

$$\sigma_0 = \sigma_{ref}\,\mathcal{H}\left(\epsilon_0^p\right)\,, \tag{16}$$

where σ_{ref} denotes a reference stress and $\mathcal{H}\left(\epsilon_0^p\right)$ is a non-dimensional hardening function that will be specified in the numerical examples that follow (see Eqs. (30) and (34)). Therefore, by combination of Eqs. (13), (15), (16), and after some algebra, the following flow stress results

$$\sigma_{flow} = \sigma_{ref}\,\sqrt{\mathcal{H}^2\left(\epsilon_0^p\right) + \ell_p\,\eta^p}\,, \tag{17}$$

where

$$\ell_p = M^2\,\bar{r}\,\beta^2\left(\frac{\mu}{\sigma_{ref}}\right)^2 b \simeq 18\,\beta^2\left(\frac{\mu}{\sigma_{ref}}\right)^2 b\,, \tag{18}$$

is a parameter with the units of length that introduces another intrinsic material length scale in the model. According to Eq. (18) and for $\mu/\sigma_{ref} \simeq 100$, typical values of ℓ_p are of the orders of microns, which is in fact the length scale where size effects are not negligible in experimental evidence. Eq. (17) introduces a correction of the conventional tensile flow stress dependent on the product $\ell_p\,\eta^p$. In the case where the length scale of the plastic deformation gradients is much larger than ℓ_p, η^p is much smaller than the plastic internal length, so the product $\ell_p\,\eta^p$ is negligible and $\sigma_{flow} \to \sigma_0$. On the other hand, if the variations of the plastic strain field are not negligible at a length of the order of ℓ_p (or less), $\sigma_{flow} > \sigma_0$ leading to a size-dependent strengthening effect.

According to Huang et al. (2004), a suitable expression for the *effective plastic strain gradient* η^p can be derived from the Nye's dislocation tensors $\boldsymbol{\chi}$. This tensor measures the incompatibility of the plastic deformation as follows

$$\boldsymbol{\chi} = -\mathrm{curl}\left[\boldsymbol{\varepsilon}^p\right]^T\,.$$

The equivalent plastic strain gradient can be then defined as the quadratic invariant of $\boldsymbol{\chi}$, i.e.

$$\eta^p = \sqrt{\boldsymbol{\chi} : \boldsymbol{\chi}}\,. \tag{19}$$

3. Numerical implementation

The problem stated in the previous section consists of a system of three partial differential equations, the balance of linear momentum Eq. (1) and the two averaging Eqs. (9). An iterative staggered approach is used to solve the governing coupled equations. Under this framework, for each time increment, the partial differential equations are solved sequentially assuming that they are uncoupled. In this way, the solution of each equation provides a correction for its relevant primary unknown (e.g. the strain field for Eq. (1) and the non-local plastic variables for Eqs. (9)). This sequential solution is carried out iteratively, employing a fixed-point iteration scheme, until the correction of the unknown fields between two consecutive iterations becomes smaller than a small tolerance, such that the solution coincides with the one obtained with a monolithic approach (Steinke et al., 2017). As demonstrated in Boeff et al. (2015) and Magri et al. (2021), combining iterative staggered schemes with solvers based on Fast Fourier Transforms provides efficient algorithms for the solution of non-local damage mechanics in the field of computational homogenization. FFT based homogenization, firstly introduced in the 90s (Moulinec and Suquet, 1994, 1998), have demonstrated to be an efficient alternative to the Finite Element Method. Typical advantages related to FFT-based solvers are that periodic boundary conditions are imposed intrinsically and digital images of real microstructures can be directly used without the need of meshing. In addition, direct comparisons with FE solvers revealed that FFT solvers can be computationally faster especially in problems characterized by a large number of unknowns (Lucarini and Segurado, 2019c). In this work, the iterative FFT-algorithm proposed in Magri et al. (2021) is first extended to incorporate the considered strain gradient plasticity model and is used thereon as the numerical framework to study the size effects in particle reinforced metal matrix composites. The solving scheme including the gradient plasticity model implementation will be presented in this section along with the discretized form of the governing equations.

3.1. Governing equations in incremental form

The rate form of the constitutive equations of the modified GTN model is integrated following the Euler Method. Assuming a loading history of the problem defined on the time interval $[t_0, t_f]$, we then divide it in N_t increments, $\Delta t_n = (t_{n+1} - t_n)$, so that the discretized fields read

$$(\bullet)|_n = (\bullet)\left(t = t_n\right), \qquad \Delta(\bullet) = (\bullet)|_{n+1} - (\bullet)|_n \qquad n = 0,\ 1,\ \dots\ N_t - 1. \tag{20}$$

For any time (or load) increment , the incremental form of the problem yields to these balance equations

$$\operatorname{div}\left[\boldsymbol{\sigma}|_{n+1}\right] = \vec{0}, \tag{21a}$$

$$\left.\overline{\epsilon_0^p}\right|_{n+1} - \operatorname{div}\left[\ell_d^2\left(\vec{x}\right)\ \nabla\left.\overline{\epsilon_0^p}\right|_{n+1}\right] = \left.\epsilon_0^p\right|_{n+1}, \tag{21b}$$

$$\left.\overline{\epsilon_V^p}\right|_{n+1} - \operatorname{div}[\ell_d^2\left(\vec{x}\right)\ \nabla\overline{\epsilon_V^p}|_{n+1}] = \epsilon_V^p|_{n+1}, \tag{21c}$$

with the constitutive laws

$$\boldsymbol{\sigma}|_{n+1} = \boldsymbol{\sigma}|_n + K\left(\vec{x}\right)\ \operatorname{tr}\left[\Delta\boldsymbol{\varepsilon} - \Delta\boldsymbol{\varepsilon}^p\right]\boldsymbol{I} + 2\,\mu\left(\vec{x}\right)\ \operatorname{dev}\left[\Delta\boldsymbol{\varepsilon} - \Delta\boldsymbol{\varepsilon}^p\right], \tag{22a}$$

$$\Delta\boldsymbol{\varepsilon}^p = \Delta\lambda\ \left[\left.\frac{\partial\phi}{\partial p}\right|_{n+1}\left.\frac{\partial p}{\partial\boldsymbol{\sigma}}\right|_{n+1} + \left.\frac{\partial\phi}{\partial s}\right|_{n+1}\left.\frac{\partial s}{\partial\boldsymbol{\sigma}}\right|_{n+1}\right], \tag{22b}$$

$$\Delta\epsilon^p = \frac{\boldsymbol{\sigma}|_{n+1} : \Delta\boldsymbol{\varepsilon}^p}{\left(1 - f|_{n+1}\right)\ \sigma_{flow}\left(\left.\epsilon_0^p\right|_{n+1}, \eta^p|_n\right)}, \tag{22c}$$

$$\Delta f = \mathcal{A}_N\left(\left.\overline{\epsilon_0^p}\right|_{n+1}\right)\Delta\overline{\epsilon_0^p} + \left(1 - f|_{n+1}\right)\ \Delta\overline{\epsilon_V^p}, \tag{22d}$$

and $\Delta\lambda$ such that

$$\phi = \left(\frac{s|_{n+1}}{\sigma_{flow}\left(\left.\epsilon_0^p\right|_{n+1}, \eta^p|_n\right)}\right)^2 + 2\ f_*|_{n+1}\ q_1\cosh\left(-\frac{3}{2}\frac{q_2\ p|_{n+1}}{\sigma_{flow}\left(\left.\epsilon_0^p\right|_{n+1}, \eta^p|_n\right)}\right) - \left(1 + q_1^2\ f_*|_{n+1}^2\right) = 0. \tag{22e}$$

The problem is completed by the choice of the following initial conditions

$$\boldsymbol{\sigma}|_{t=t_0} = \boldsymbol{\sigma}_0, \quad \boldsymbol{\varepsilon}^p|_{t=t_0} = \boldsymbol{\varepsilon}_0^p, \quad \left.\epsilon_0^p\right|_{t=t_0} = \epsilon_0^p, \quad f|_{t=t_0} = f_0.$$

Note that the functional dependence of σ_{flow} is written in terms of $\eta^p|_n$ instead of $\eta^p|_{n+1}$, which renders the numerical method semi-implicit. This approximation is generally taken in the numerical solution of lower-order SGP models since it allows for a straightforward implementation of Eq. (21a) using similar solving algorithms to the one employed for local plasticity models (see Haouala et al. (2020) for instance). Eqs. (21) are solved for a prescribed mixed loading history given by a combination of components of the macroscopic strain $\mathbf{E}|_{n+1}$ and stress $\boldsymbol{\Sigma}|_{n+1}$ tensors, such that

$$E_{ij}|_{n+1} = \langle E_{ij}(t)\rangle = \frac{1}{\Omega}\int_\Omega \varepsilon_{ij}|_{n+1}\left(\vec{x}\right)\ \mathrm{d}V, \qquad \Sigma_{IJ}|_{n+1} = \langle\sigma_{IJ}(t)\rangle = \frac{1}{\Omega}\int_\Omega \sigma_{IJ}|_{n+1}\left(\vec{x}\right)\ \mathrm{d}V,$$

where i, j and I, J refer, respectively, to the components in which macroscopic strain or stress are prescribed (with $i, j \cap I, J = \emptyset$). In addition, periodic boundary conditions are imposed for all the solution variables

$$\boldsymbol{\varepsilon}(\vec{x}) = \boldsymbol{\varepsilon}(\vec{x} + \vec{n}L), \tag{23a}$$

$$\overline{\epsilon_0^p}(\vec{x}) = \overline{\epsilon_0^p}(\vec{x} + \vec{n}L), \tag{23b}$$

$$\overline{\epsilon_V^p}(\vec{x}) = \overline{\epsilon_V^p}(\vec{x} + \vec{n}L), \tag{23c}$$

with $\vec{n}L$ referring to any vector with components obtained as the product of an integer number by the periodicity of the RVE, i.e. L.

3.2. The iterative staggered algorithm

At increment n, assuming the relevant field variables to be known, the incremental problem (21) consists in finding $\boldsymbol{\varepsilon}^p|_{n+1}$, $\overline{\epsilon_0^p}$, and $\overline{\epsilon_V^p}$ with a macroscopic prescribed state given by a combination of strain and stress components $E_{ij}|_{n+1}$ and $\Sigma_{IJ}|_{n+1}$. The adopted iterative staggered algorithm schematizes as follows

Initialize the solution fields:

– $\boldsymbol{\varepsilon}|_{n+1}^{(0)} = \boldsymbol{\varepsilon}|_n$, $\left.\overline{\epsilon_0^p}\right|_{n+1}^{(0)} = \left.\overline{\epsilon_0^p}\right|_n$, $\left.\overline{\epsilon_V^p}\right|_{n+1}^{(0)} = \left.\overline{\epsilon_V^p}\right|_n$

Compute the effective plastic strain gradient, η^p, from $\boldsymbol{\varepsilon}^p|_n$, Eq. (19) (Section 3.4)

Iterate over $k = 0, 1, \dots$ until convergence

(a) solve the purely mechanical problem via the FFT-Galerkin algorithm:
- assign $\overline{\epsilon_0^p}|_{n+1} = \overline{\epsilon_0^p}|_{n+1}^{(k)}$ and $\overline{\epsilon_V^p}|_{n+1} = \overline{\epsilon_V^p}|_{n+1}^{(k)}$ in Eq. (22d)
- compute $\boldsymbol{\epsilon}|_{n+1}^{(k+1)}$ by solving (21a) along with Eqs. (22) and Eq. (17)
- save the local plastic variables $\epsilon_0^p|_{n+1}^{(k+1)}$ and $\epsilon_V^p|_{n+1}^{(k+1)}$

(b) solve the non-local averaging equations in FFT:
- assign $\epsilon_0^p|_{n+1} = \epsilon_0^p|_{n+1}^{(k+1)}$ in Eq. (21b)
- assign $\epsilon_V^p|_{n+1} = \epsilon_V^p|_{n+1}^{(k+1)}$ in Eq. (21c)
- compute $\overline{\epsilon_0^p}|_{n+1}^{(k+1)}$ by solving Eq. (21b)
- compute $\overline{\epsilon_V^p}|_{n+1}^{(k+1)}$ by solving Eq. (21c)

(c) check convergence:
- if (max{err_1, err_2, err_3} < tolerance): increment completed
- else: $k = k + 1$ and go to (a)

where
- $err_1 = \frac{\max\left[\boldsymbol{\epsilon}|_{\boldsymbol{n+1}}^{(\boldsymbol{k+1})} - \boldsymbol{\epsilon}|_{\boldsymbol{n+1}}^{(\boldsymbol{k})}\right]}{\langle \boldsymbol{\epsilon}|_{\boldsymbol{n+1}}^{(\boldsymbol{k+1})} \rangle}$
- $err_2 = \frac{\|\overline{\epsilon_0^p}|_{n+1}^{(k+1)} - \overline{\epsilon_0^p}|_{n+1}^{(k)}\|}{\langle \overline{\epsilon_0^p}|_{n+1}^{(k+1)} \rangle}$
- $err_3 = \frac{\|\overline{\epsilon_V^p}|_{n+1}^{(k+1)} - \overline{\epsilon_V^p}|_{n+1}^{(k)}\|}{\langle \overline{\epsilon_V^p}|_{n+1}^{(k+1)} \rangle}$

At the core of the algorithm two distinct spectral solvers are used for the solution of the governing equations of the problem. The first type of solver is an FFT-Galerkin algorithm (Vondřejc et al., 2014; Zeman et al., 2017) exploited for the solution of the non-linear Eq. (21a), which has the mathematical structure of a conventional mechanical problem within this iterative solver. This Fourier–Galerkin solver is complemented with the technique proposed by Lucarini and Segurado (2019a) for prescribing, without requiring additional iterations, macroscopic loading states that combine strain and stress components. On the other hand, the averaging equations ((21)b-c) are both solved numerically in Fourier space with a conjugate-gradient based algorithm (Magri et al., 2021). Further details on the solving algorithms are left in the Appendix for completeness.

3.3. Spatial discretization and discrete derivative rule

The spatial discretization of Eqs. (21) follows the standard procedure adopted for spectral solvers. In micromechanical analysis, the simulation domain is typically a periodic RVE embedded in a cuboidal domain with edges lengths L_1, L_2, L_3. Such an RVE is discretized with a regular array of $N_1 \times N_2 \times N_3$ voxels, where each voxel belongs to any of the phases represented. The unknown discrete fields correspond to their values at the center of each cell, with position $\vec{x}$ given by

$$x_i = (\frac{1}{2} + n_i)\frac{L_i}{N_i}, \qquad i = 1,2,3 \text{ and } n_i \in [0, N_i - 1]\,.$$

The Fourier transform of the discrete field is taken as the discrete Fourier transform. The corresponding $N_1 \times N_2 \times N_3$ discrete frequencies in Fourier space, $\vec{\xi}$, are given by

$$\xi_i = \frac{2\pi}{L_i}\begin{cases} n_i - \dfrac{(N_i - 1)}{2} & \text{if } N_i \text{ odd} \\ n_i - \dfrac{N_i}{2} & \text{if } N_i \text{ even} \end{cases} \qquad \text{for} \quad i = 1,2,3 \text{ and } n_i \in [0, N_i - 1]\,. \tag{24}$$

Using the properties of the Fourier transforms, the partial derivative of a given generic function φ in the real space can be easily calculated given its Fourier transform $\mathcal{F}[\varphi]$ as

$$\mathcal{F}\left[\frac{\partial \varphi}{\partial x_i}\right] = \mathrm{i}\,\xi_i \mathcal{F}[\varphi]\,, \tag{25}$$

where $\mathcal{F}$ is the Fourier transform operator while i indicates the imaginary unit. If the field φ exhibits strong spatial discontinuities, the usage of the standard derivative rule Eq. (25) might give rise to noisy solutions. Such a behavior is typical of problems with large phase property contrasts, especially near the phase boundaries, or in the case where the field to be derived drops sharply to zero in some regions, as it happens for instance for the plastic strain in the elastic reinforcements of a composite materials.

To alleviate this numerical noise, we adopt the modified derivative rule proposed by Willot (2015) for a purely mechanical problem. This alternative definition – which is based upon the application of a finite difference scheme in the real space for a spatial derivative – substitutes the classical continuum derivative Eq. (25) with

$$\mathcal{F}\left[\frac{\partial \varphi}{\partial x_i}\right] = \mathrm{i}\,k_i(\vec{\xi})\,\mathcal{F}[\varphi]\,, \tag{26}$$

where $\vec{k}$ is a modified version of the frequency vector that reads

$$k_i(\vec{\xi}) = \frac{1}{4}\tan\left(\frac{\hat{\xi}_i}{2}\right)(1+e^{\hat{\xi}_1})(1+e^{\hat{\xi}_2})(1+e^{\hat{\xi}_3}),$$

with $\hat{\xi}_i = \xi_i\, L_i/(2\pi N_i)$. This modified derivative is exploited for the solution of Eq. (21a) only, (see Appendix A). On the other hand, the numerical solution of Eqs. ((21b)-c) in Fourier space is carried out using the standard form Eq. (25).

3.4. Calculation of the equivalent plastic strain gradient

In the MSGP model considered here, size effects in the mechanical response are introduced through the dependence of η^p, the scalar measure of the plastic strain gradient, in the modified flow stress Eq. (17). η^p is selected here as a quadratic invariant of the Nye's dislocation tensor χ in Eq. (19). According to the geometrical considerations of Nye (1953), χ quantifies the incompatibility of the plastic strain tensor and takes the following expression

$$\chi = -\mathrm{curl}\left[\varepsilon^p\right]^T,$$

which is computed operatively as

$$\chi_{ij} = -\epsilon_{irs}\frac{\partial \varepsilon^p_{js}}{\partial x_r}, \tag{27}$$

where ϵ denotes the Levi-Civita permutation tensor. The calculation of the components of the plastic strain gradient can be easily carried out in Fourier space by using the discrete derivative rule (26) in order to increase the accuracy in the calculation of χ and limit the emergence of Gibbs oscillations at phase interfaces (see Haouala et al. (2020), Berbenni et al. (2014), Brenner et al. (2014), Lebensohn and Needleman (2016) and Marano et al. (2019) for instance). However, the calculation of spatial derivatives using a finite difference formula should be handled carefully if applied to discontinuous fields. The numerical derivative computed with this strategy indeed depends on the spatial discretization leading to a non-objective calculation of χ as demonstrated in Appendix C. Therefore, the implementation of SGP models in FFT-based solvers can lead to inaccurate results depending on how plastic strain gradients are computed numerically.

In this paper, we propose an alternative numerical strategy for the calculation of plastic strain gradients that produces grid independent results. The idea is to apply an implicit gradient regularization to each component of the plastic strain gradient and then apply the curl operation to these fields. The regularization of each plastic strain gradient component follows Eq. (9) as

$$\overline{\frac{\partial \varepsilon^p_{js}}{\partial x_r}} - \ell_\varepsilon^2\nabla^2\left[\overline{\frac{\partial \varepsilon^p_{js}}{\partial x_r}}\right] = \frac{\partial \varepsilon^p_{js}}{\partial x_r}, \tag{28}$$

where ℓ_ε is the relevant characteristic length of the regularization, which is assumed to be homogeneous throughout the domain. The components of the plastic strain gradient appearing on the right-hand side of Eq. (28) are calculated in Fourier space using the centered discrete derivative rule (see Willot (2015) for details)

$$\frac{\partial \varepsilon^p_{js}}{\partial x_r} = \mathcal{F}^{-1}\left[\mathrm{i}\sin\left(\hat{\xi}_r\right)\,\mathcal{F}\left[\varepsilon^p_{js}\right]\right],$$

Finally, the equivalent plastic strain gradient η^p is estimated from the Nye's dislocation tensor

$$\chi_{ij} = -\epsilon_{irs}\overline{\frac{\partial \varepsilon^p_{js}}{\partial x_r}}, \tag{29}$$

This alternative strategy for computing the dislocation tensor is objective and its use in the considered MSGP model produces grid independent numerical results as demonstrated by the convergence study reported in Appendix C. It is worth noting that Eq. (28) introduces a further length parameter into the model. Nevertheless, contrary to ℓ_p and ℓ_d, ℓ_ε merely represents a numerical parameter for the objective calculation of plastic strain gradients and is not associated to any physical process. Its numerical value, in the simulations that follow, will be selected equal to the size of a few voxels in order for the implicit regularization to be effective and, at the same time, to provide a limited smoothening of the original discrete derivatives. The numerical solution of Eq. (28) is carried out in Fourier space, as pursued for the Helmholtz-type equations ((21b)-c). In this case, the choice of a homogeneous ℓ_ε speeds up significantly the calculations since it allows for a direct solution of the problem without the need of resorting to iterative solvers.

4. Numerical results

4.1. Representation of the microstructure and material parameters

The generation of the three-dimensional RVEs used in the numerical simulations follows the methodology described in Segurado and Llorca (2002). A cubic unit cell of size $L\times L\times L$ is filled with 30 non-overlapping identical spheres representing the reinforcement. This number of particles is sufficient to have a statistically isotropic arrangement of the spherical inclusions. The position of the

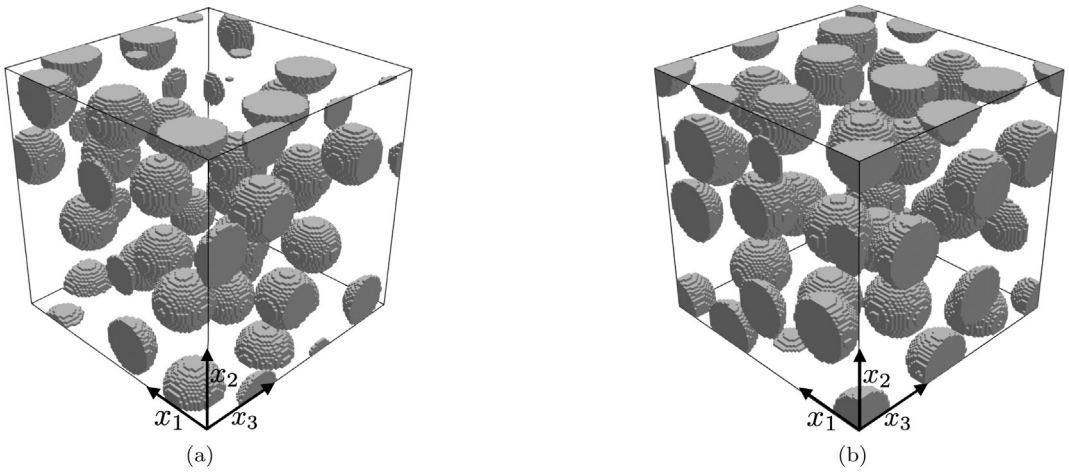

Fig. 2. Periodic multi-particle RVEs adopted in the 3D numerical simulations in the case of (a) 15% and (b) 20% volume fraction of reinforcing particles. The grid resolution is 100^3 voxels for a total of 1×10^6 grid points.

particles is generated using a Random Sequential Adsorption algorithm, in which the centers of spheres of radius R are introduced sequentially and randomly. In this algorithm, a new generated particle is accepted if the distance between its center and the one of all the previous particles is greater that $2.07R$, in order to have approximately a minimum of two voxels representing the matrix between two particles.

A voxel-based digital representation of the RVE is then generated by rastering the considered microstructure using the same number of grid points along the three principal axis. The digital voxel-based unit cells used in this study are reported Fig. 2.

The material parameters are set to mimic the response of an Aluminum alloy reinforced with SiC particles. In particular, the elastic properties of the matrix are selected as $E_M = 70$ GPa and $\nu_M = 0.33$ while $E_S = 427$ GPa and $\nu_S = 0.17$ are assigned to the elastic reinforcements. The parameters of the GTN model for the composite matrix are set as $q_1 = 1.5$, $q_2 = 1$, $f_C = 0.15$, $f_F = 0.25$, $f_N = 0.08$, $\epsilon_N = 0.1$, and $s_N = 0.05$. The initial void volume fraction is zero and microvoids will nucleate according to Eq. (8). The non-dimensional hardening function $\mathcal{H}\left(\epsilon_0^p\right)$ is specified as a power law

$$\mathcal{H}\left(\epsilon_0^p\right) = \frac{\sigma_Y}{\sigma_{ref}}\left(1 + \frac{E_M\,\epsilon_0^p}{\sigma_Y}\right)^N, \tag{30}$$

with $\sigma_Y = 200$ MPa, $\sigma_{ref} = 250$ MPa, and $N = 0.1$.

In the GTN model, the local bearing capacity of the matrix material is lost as soon as the damage indicator f_* equals f_V^*. If such a condition is attained, the convergence of the FFT-Galerkin scheme used to solve Eq. (21a) is compromised since the contrast between the stiffness of matrix and inclusions becomes too high. Therefore, for numerical convenience, the upper limit of the damage variable is limited to $f_* = 0.95\, f_V^* = 0.63$. Accordingly, a low residual stress capacity is left to the "fully damaged" material matrix. To prevent spurious propagation of inelastic non-local variables in the region occupied by the elastic particles when solving Eqs. (9), the length parameter in the elastic phases ℓ_d^S is taken such that $\ell_d^S/\ell_d^M = 0.02$. In this way, according to Eq. (10), ℓ_d is defined as function of ℓ_d^M only. Therefore, for the sake of readability, symbol ℓ_d will be directly used in place of ℓ_d^M in what follows, being the latter the only relevant parameter for the non-local regularization of damage. The length-parameter introduced in the definition of the objective plastic strain gradient is taken as $\ell_\varepsilon = 0.02L$ for all the simulations. This value corresponds to two voxels length, which is the minimum number of elements suggested in Miehe et al. (2015), in the framework of phase-field fracture, for the fracture length scale parameter in order to represent accurately the solution of the Helmholtz equation.

Unless otherwise specified, in the numerical simulations that follow, the RVE is subjected to a uniaxial tensile loading in which a macroscopic strain is prescribed in the direction x_1, while a stress free condition is enforced in the remaining components

$$\boldsymbol{E} = \begin{pmatrix} E_{11} & * & * \\ * & * & * \\ * & * & * \end{pmatrix} \quad \text{and} \quad \boldsymbol{\Sigma} = \begin{pmatrix} * & 0 & 0 \\ 0 & 0 & 0 \\ 0 & 0 & 0 \end{pmatrix}.$$

4.2. Parametric study of the size dependent strengthening and ductility

The goal of this section is to show the influence of the considered non-local extensions on the proposed model, i.e. the modified MSGP flow stress (17) and the Helmholtz-type Eqs. (9). Such non-local equations introduce multiple length-scales into the model through the intrinsic length parameters ℓ_p and ℓ_d. The former one modulates the plastic strain gradient induced strengthening in the material matrix. On the other hand, ℓ_d controls the spreading of the damage related plastic variables thus influencing the overall

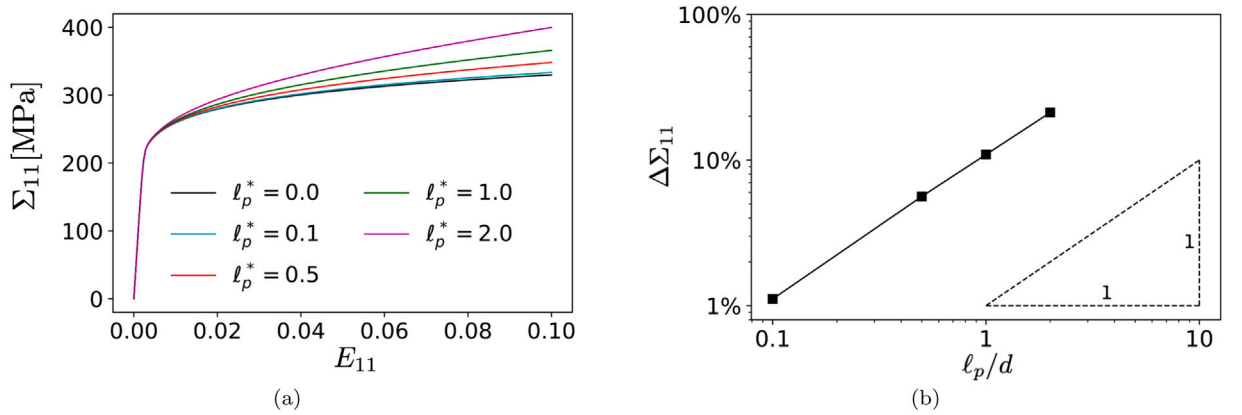

Fig. 3. (a) Plot of the average stress component Σ_{11} against the average strain component E_{11} for different values of the adimensional parameter ℓ_p^*. (b) Log–log plot of the relative strengthening $\Delta\Sigma_{11}$ introduced by the considered MSGP model as a function of the adimensional parameter $\ell_p^* = \ell_p/d$. The reported results are obtained for a RVE containing 20% volume fraction of reinforcing particles.

ductility of the composite. To provide a general analysis of the impact of the two non-local mechanisms separately, the first two sets of numerical simulations that follow will be parametrized with respect to the non-dimensional parameters

$$\ell_p^* = \frac{\ell_p}{d} \qquad \text{and} \qquad \ell_d^* = \frac{\ell_d}{d}, \tag{31}$$

with d indicating the particle diameter. Therefore, the change in strengthening and ductility promoted by the considered non-local theories will be directly linked to the particle size as usually assessed in the experimental studies.

4.2.1. Particle size induced strengthening

The impact of the MSGP model on the composite material is firstly analyzed by neglecting the mechanical degradation associated with damage. To suppress damage nucleation, parameter f_N is set to zero and, therefore, the composite matrix behaves as an elasto-plastic material without softening. Fig. 3a represents the stress strain curves obtained from the simulations for different values of the adimensional parameter ℓ_p^*. The numerical results highlight a prominent size effect in the macroscopic response of the metal matrix composite in view of Eq. (31): the lower the particle size (i.e. higher ℓ_p^*), the larger the simulated macroscopic stress. By comparing the reference solution $\ell_p^* = 0$ with the other curves, it can be seen that the particle size basically induces a negligible strengthening if the particle diameter is much larger than the parameter ℓ_p (i.e. $d > \ell_p/10$). On the other hand, when the particle diameter approaches ℓ_p the composite strength increases significantly up to about 20% in case of $\ell_p = 2d$. A quantitative evaluation of the strengthening induced by the MSGP model can be calculated as the relative increment in simulated stress (at the end of each simulation) with respect to the one obtained in the case of conventional plasticity, i.e.

$$\Delta\Sigma_{11}(\ell_p^*) = \frac{\Sigma_{11}(\ell_p^*) - \Sigma_{11}(\ell_p^* = 0)}{\Sigma_{11}(\ell_p^* = 0)}. \tag{32}$$

These results are represented in Fig. 3b using a $log - log$ graph, showing that the strengthening scales linearly with ℓ_p/d, similarly to the results obtained with other SGP models (see Bassani et al. (2001) for instance).

Fig. 4 represents the spatial distribution of the equivalent plastic strain gradient η^{p*} in the case of the maximum ℓ_p^* simulated, which corresponds to the smallest particle size $d = \ell_p/2$. It can be observed that the plastic strain gradient localizes in regions touching the particle interfaces. In the opposite case, when $\ell_p^* = 0$, plastic strain gradient effects are neglected in the modified flow stress.

Fig. 5 reports the spatial distribution of the equivalent Mises stress in the material matrix for different values of ℓ_p^* at the end of each simulation. As observed in Fig. 3a, the RVEs containing particles with small diameters are capable of sustaining higher stress states. In addition to that, a smaller particle diameter induces a different stress distribution in the material matrix with a higher stress concentration. By comparing Fig. 5c with Fig. 4, i.e. the one reporting the distribution of the equivalent plastic strain gradient for the same ℓ_p^*, it can be observed that the distribution of the Mises stress basically coincides with the one of η^p. Therefore, for small particles the equivalent plastic strain gradient produces a dominant effect in the modified flow stress Eq. (17).

4.2.2. Size dependent ductility

In this second set of numerical simulations we aim at evaluating the impact of the non-local regularization of damage defined by Eqs. (9). In order to focus specifically on damage regularization, strain gradient plasticity effects are switched off by prescribing $\ell_p = 0$. Fig. 6a collects the macroscopic stress strain curves obtained with different values of the non-dimensional parameter ℓ_d^*. Note that the material behavior of the composite matrix in the case of $\ell_d^* = 0$ coincides with the classical GTN model (Tvergaard and Needleman, 1984) since $\overline{\epsilon_0^p} = \epsilon_0^p$ and $\overline{\epsilon_V^p} = \epsilon_V^p$. As expected, parameter ℓ_d^* influences significantly the overall ductility of the

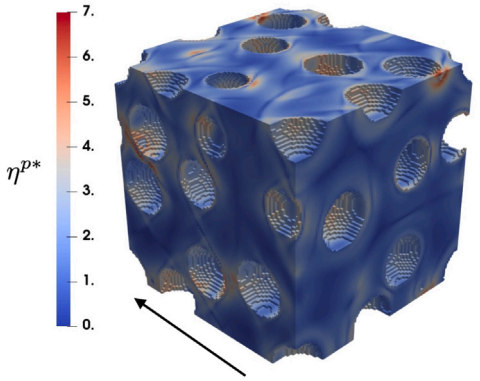

Fig. 4. Spatial distribution of the non-dimensional equivalent plastic strain gradient η^{p*} obtained as $\eta^{p*} = L\,\eta^{p}$ for $\ell_p^* = 2.0$ (the black arrow indicates the loading direction). The reported results are obtained for a RVE containing 20% volume fraction of reinforcing particles.

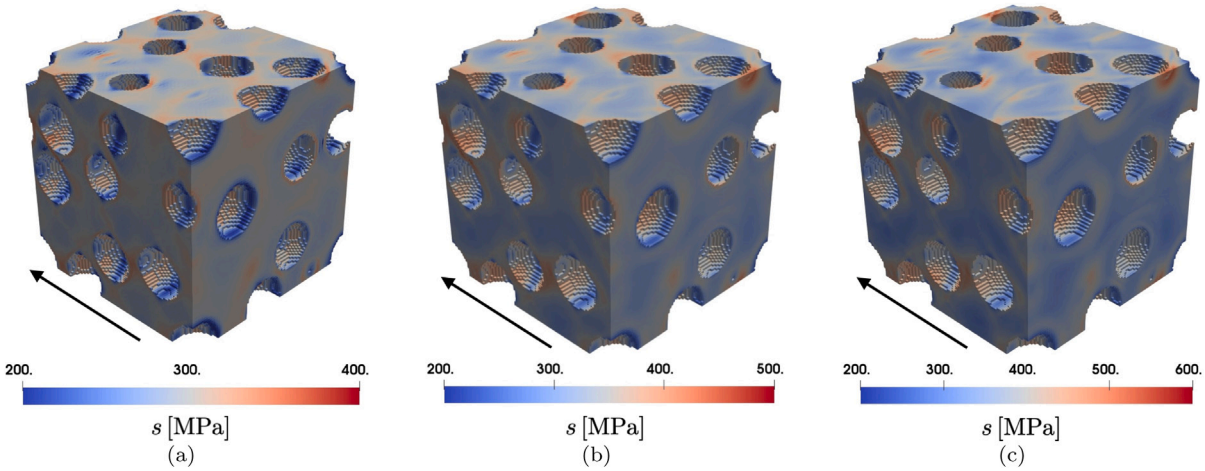

Fig. 5. Mises equivalent stress in the RVE at $E_{11} = 0.1$ for (a) $\ell_p^* = 0.0$, (b) $\ell_p^* = 1.0$, and (c) $\ell_p^* = 2.0$. Note that colorbars have been reported with different scales to better capture the stress distribution in each case. The black arrow indicates the loading direction.

metal matrix composite: a higher ductility results for higher values of ℓ_d^*. From the reported results, it can be noted that all the simulations stop before the final failure of a material point is reached, i.e. before the macroscopic stress tends to zero. This occurs because of lack of convergence of the FFT solver after a significant damage evolution in the matrix in spite of the restriction made on f_V^*. As demonstrated in Magri et al. (2021), a more relaxed (but less accurate) choice of f_V^* would allow for the simulation of the complete failure of the RVE induced by the propagation of damage following a percolation path compatible with the reinforcements. Therefore, the assumption made here on f_V^* is a compromise between accuracy of the solution – since f_V^* has not been penalized excessively – and numerical convergence – as the FFT solver allows capturing the stress softening regime corresponding to incipient macroscopic fracture.

A quantitative comparison of the simulated composite ductility, as a function of ℓ_d^*, can be drawn by computing the so-called ultimate composite ductility E_u. The latter is defined as the macroscopic strain corresponding to the maximum simulated composite stress Σ_u, i.e. the one identified by the condition $\mathrm{d}\Sigma_{11}/\mathrm{d}E_{11} = 0$. Fig. 6b plots the increment, using a log–log scale, in the ultimate composite ductility calculated relative to the case with $\ell_d^* = 0$

$$\Delta E_u(\ell_d^*) = \frac{E_u(\ell_d^*) - E_u(\ell_d^* = 0)}{E_u(\ell_d^* = 0)}\,. \tag{33}$$

Fig. 7 reports the spatial distribution of the non-local equivalent plastic strain in the matrix, $\overline{\epsilon_0^p}$, for three different particles sizes (similar considerations can be made for $\overline{\epsilon_V^p}$). For smaller ℓ_d^* (larger size of the reinforcements) the spatial spreading of the plastic variable is small (Eq. (9a)) and damage bands are small relative to the particle size (see Fig. 8a–b). In the case of $\ell_d^* = 0$ the non-local plastic equivalent plastic strain equals the discrete local field so damage bands correspond to the size of a voxel. Accordingly, the mechanical degradation associated with the evolution of inelastic variables localizes in a small fraction of the composite matrix leading to an early macroscopic softening. On the other hand, a remarkable diffusion of $\overline{\epsilon_0^p}$ results for higher

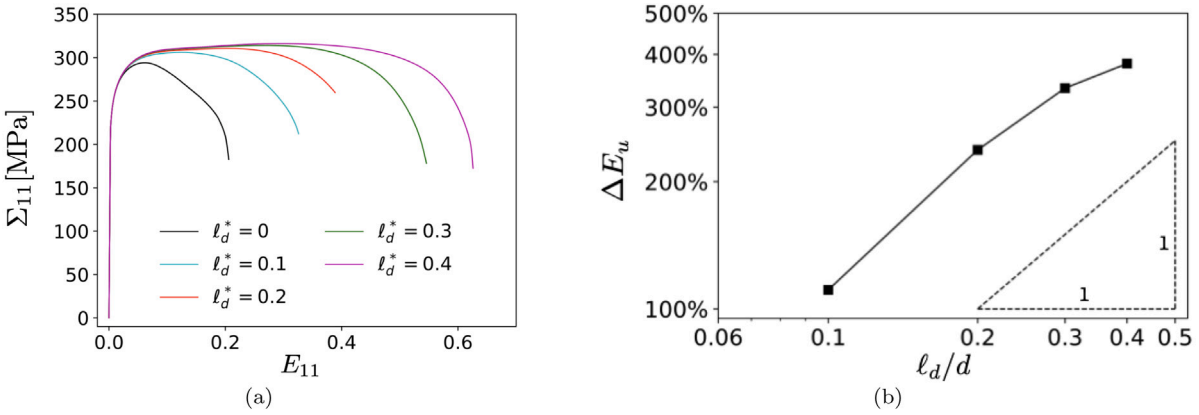

Fig. 6. (a) Plot of the average stress component Σ_{11} against the average strain component E_{11} for different values of the adimensional parameter ℓ_d^*. (b) Log–log plot of the change in ductility ΔE_u induced by the adopted damage regularization as a function of the adimensional parameter $\ell_d^* = \ell_d/d$. The reported results are obtained for a RVE containing 20% volume fraction of reinforcing particles.

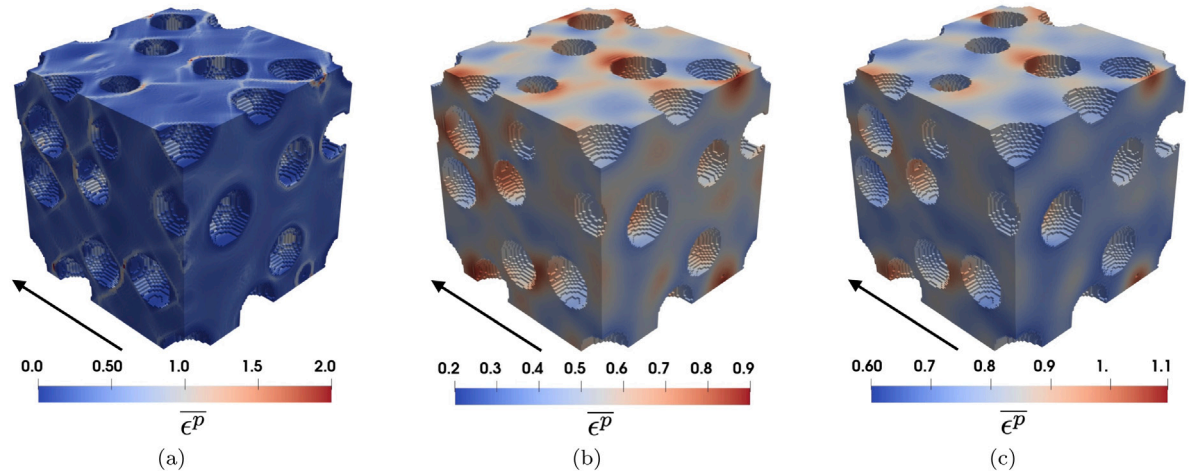

Fig. 7. Non-local equivalent plastic strain in the RVE at the end of each simulation for (a) $\ell_d^* = 0$, (b) $\ell_d^* = 0.2$, and (c) $\ell_d^* = 0.4$. Note that colorbars have been reported with different scales to better capture the strain distribution in each case. The black arrow indicates the loading direction.

values of ℓ_d^* (smaller particles size). A larger portion of the RVE matrix is, therefore, involved with damage induced mechanical degradation and the composite is capable of dissipating more mechanical energy. These conclusions are supported by the results reported in Fig. 8, which collects the distribution of the effective porosity f_* for different values of ℓ_d^*. Damage localizes in small regions in correspondence of the particle–matrix interfaces while the rest of the composite matrix experiences a limited amount of nucleated voids for small ℓ_d^* (see Fig. 8a). Conversely, a higher ℓ_d^* promotes the development of damage in a larger volume fraction of the RVE as shown in Fig. 8b–c.

4.2.3. Combined SGP and non-local damage

In this section, we evaluate the mechanical response of the metal matrix composite in the case where both the SGP model and the non-local damage regularization are active. To analyze the size dependent response of the model in terms of strengthening and ductility, the value of the characteristic length in SGP, ℓ_p, is fixed and the numerical simulations that follow are parametrized with respect to the particle diameter d and the internal length scale ℓ_d. Fig. 9 collects the simulated macroscopic strain stress curves for different particle diameters in case of $\ell_d = 1\,\mu m$ and $\ell_d = 5\,\mu m$. In both graphs, $\ell_p = 10\,\mu m$ is prescribed. A significant increase in strengthening and ductility is obtained for decreasing particle size for the two considered internal lengths of the damage regularization. Therefore, at least for the considered range of particle sizes and material parameters, the coupling between the considered non-local theories promotes a mechanical size effect of type: the smaller the reinforcements, the higher the simulated strengthening and ductility. All the experimental studies show a clear particle size effect on the strength, as captured by the combined model. On the other hand, the experimental trend observed for the ductility is not so clear and, although in many cases the ductility increases with the particle size – contrary to our model prediction – other results show almost size independent (or even decreasing)

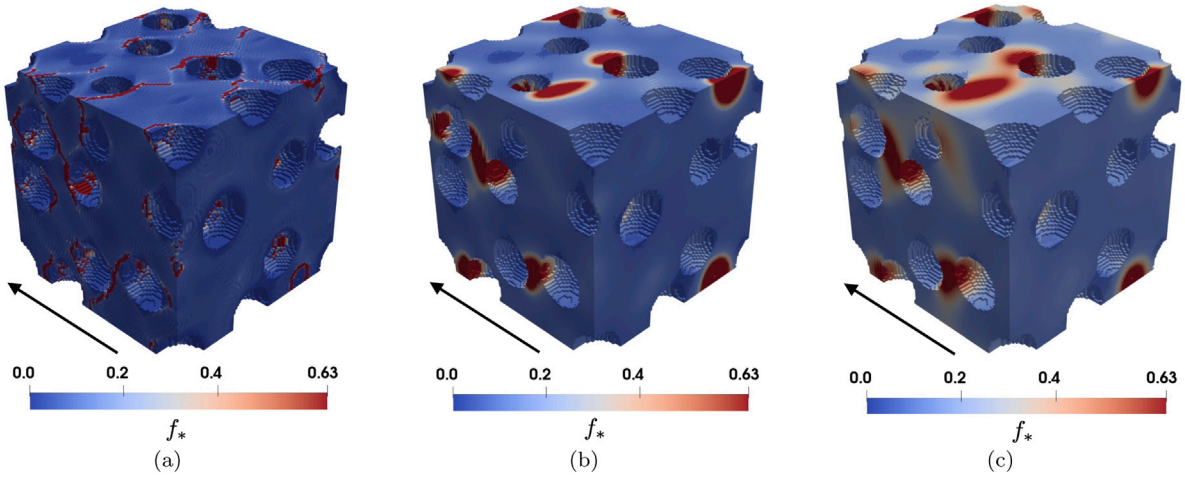

Fig. 8. Effective porosity in the RVE at the end of each simulation for (a) $\ell_d^* = 0$, (b) $\ell_d^* = 0.2$, and (c) $\ell_d^* = 0.4$. The black arrow indicates the loading direction.

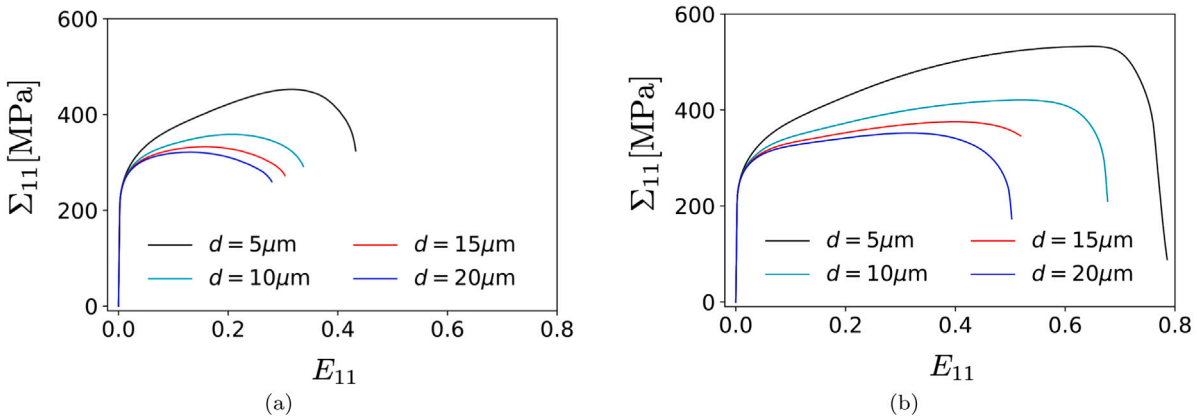

Fig. 9. Simulated macroscopic stress strain curves for different diameters d of reinforcing particles for $\ell_p = 10$ μm and in the case of (a) $\ell_d = 1$ μm and (b) $\ell_d = 5$ μm. The reported results are obtained for a RVE containing 20% volume fraction of reinforcing particles.

ductility for increasing particle size (e.g. see Al/SiC at 100 °C in Lloyd (1994)). These difference in the ductility trend can be explained by looking at the dominant damage mechanism in the composite. If either particle fracture or debonding are the main mechanisms, the broken particles and the detached regions act as large voids which promote damage growth. In this case, particles with smaller sizes lead to en early evolution of damage in the composite since the stress in the particles and at the particle/matrix interface is higher. This is the typical case at room temperature (Lloyd, 1994) where the size effect is of type "smaller is weaker". On the contrary, when the matrix yield stress is small enough, particle cracking and debonding is suppressed so that their effect in the fracture process reduces to the generation of stress concentration areas at the particle/matrix interface leading to microvoid nucleation, growth, and coalescence. This might occur, for instance, at high temperature and in this case, even if the particle size effect is small, it can show a trend of type "the smaller, the more ductile" in agreement with the predictions of this model.

Fig. 10 plots the relative ultimate composite stress $\Delta\Sigma_u$ and ductility ΔE_u obtained from the coupling between MSGP and implicit gradient regularization. By comparison between Fig. 3b and Fig. 10a, it results that the magnitude of the strengthening induced by the coupling between the MSGP model and the damage regularization is higher than the one obtained by considering the MSGP model only. Therefore, if coupled with a strain gradient model, the damage regularization impacts significantly on the composite strengthening as well, inducing a higher strengthening for increasing ℓ_d. In addition, it can also be noted that the strengthening in Fig. 10a grows slightly faster with $1/d$ than the one in Fig. 3b. Similar considerations on the simulated composite ductility: the simulated composite ductility changes considerably if the MSGP model is considered along with the non-local damage regularization (cf. Fig. 6b and Fig. 10b). In particular, the composite ductility increases if strain gradients effects are included.

4.3. Impact of stress triaxiality

For the sake of completeness, a brief analysis of the impact of the prescribed stress triaxiality – in view of the considered damage regularization – is reported in this section. To this end, three different macroscopic loading conditions have been applied to the

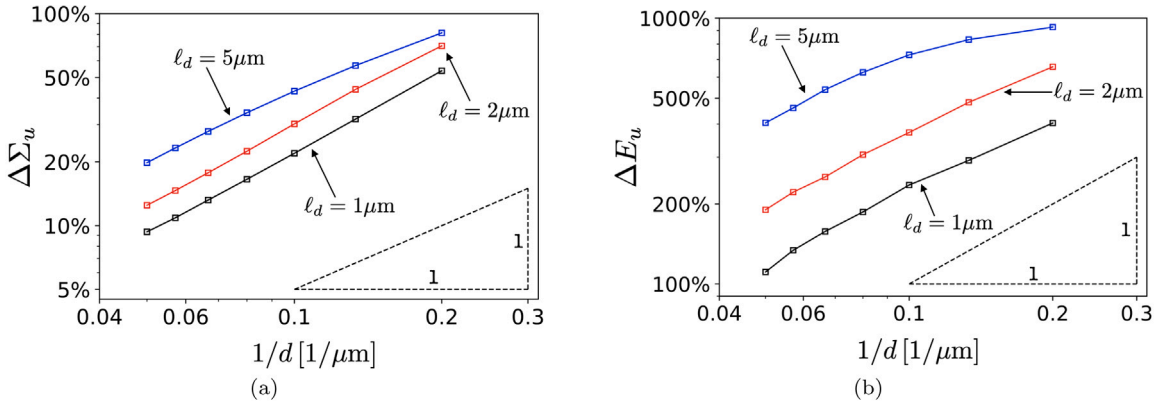

Fig. 10. Log–log plot of (a) the relative strengthening $\Delta\Sigma_u$ and (b) ductility ΔE_u as a function of $1/d$ induced by the fully-coupled model including MSGP and the damage regularization. The reported results are obtained for a RVE containing 20% volume fraction of reinforcing particles and by taking $\ell_p = 10$ μm.

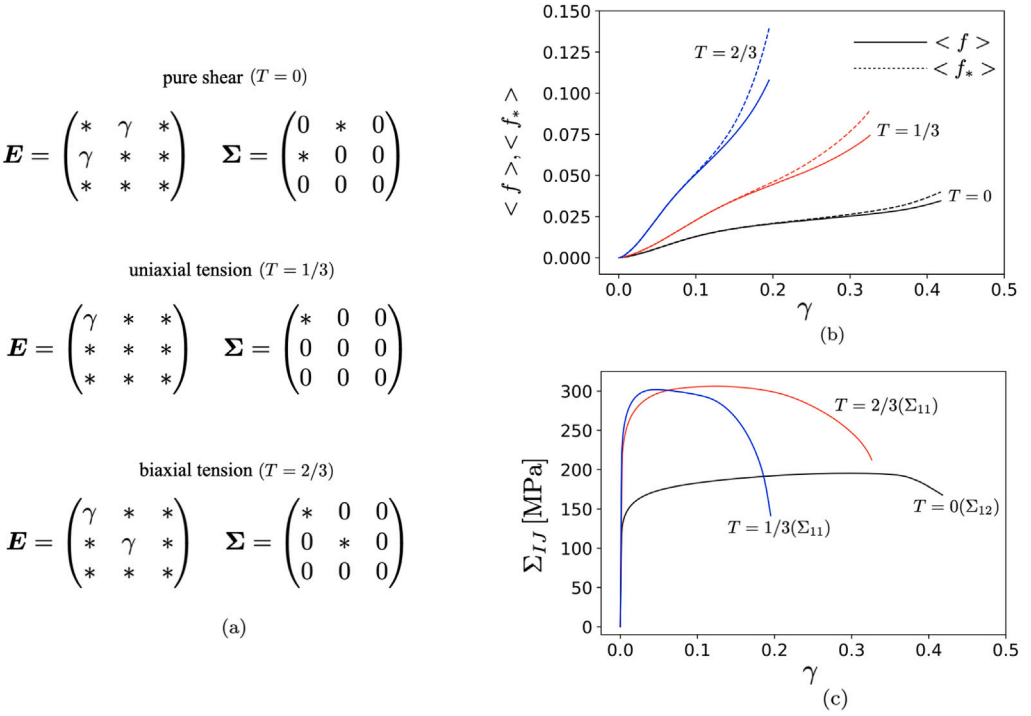

Fig. 11. (a) Macroscopic stress/strain condition used for the numerical analysis aiming at showing the impact of stress triaxiality. (b) Evolution of the average microporosity $\langle f \rangle$ and average effective microporosity $\langle f_* \rangle$ as a function of the load parameter γ. (c) Plot of the macroscopic stress components versus the load parameter γ (in parenthesis is reported the specific stress component printed in each curve). The reported results are obtained for a RVE containing 20% volume fraction of reinforcing particles along with $\ell_d^* = 0.1$ and $\ell_p^* = 0$.

particle composite as schematized in Fig. 11a. The considered mixed macroscopic loadings aim at mimic the cases of pure shear (corresponding to *macroscopic triaxiality* $T = 0$), uniaxial tension with $T = 1/3$, and biaxial tension with $T = 2/3$. Fig. 11b plots the evolution of the void volume fraction $\langle f \rangle$ and average effective porosity $\langle f_* \rangle$ as a function of the load parameter γ. The reported results reproduce the trends found in the local version of the GTN model, a higher macroscopic triaxiality promotes a faster microvoid growth. This induces a more ductile response for lower applied triaxiality, as usually expected. In addition, high stress triaxiality results in higher values of $\langle f \rangle$ in correspondence of the macroscopic coalescence condition, i.e. where $\langle f \rangle$ and $\langle f_* \rangle$ bifurcate. Similar conclusions on the simulated ductility can be drawn by the analyzing the evolution of the macroscopic stress components, as reported in Fig. 11c. The latter, confirms that higher composite ductility is obtained for lower stress triaxialities.

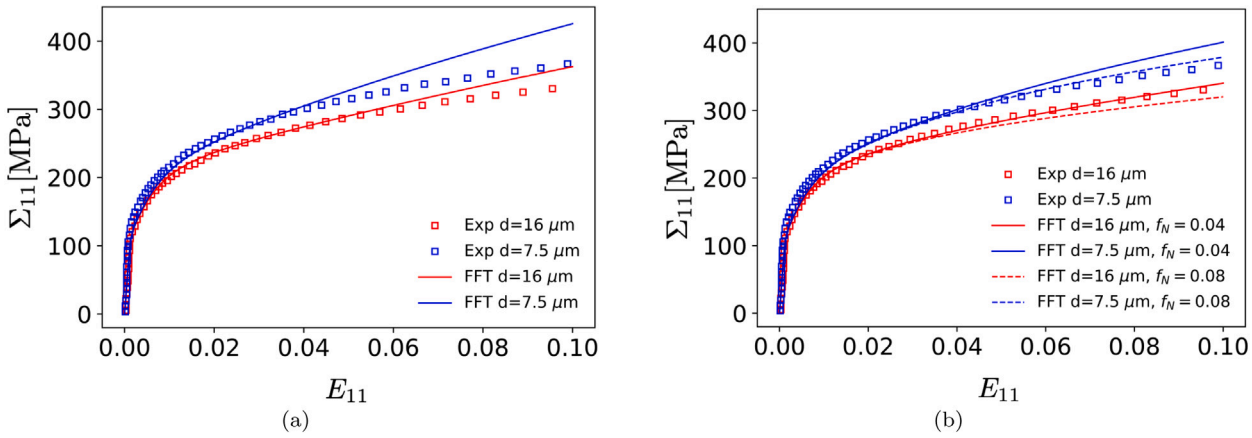

Fig. 12. Comparison between the experimental results of Lloyd (1994) and the numerical outcomes obtained with the considered extended model (a) without and (b) with the impact of damage.

4.4. Comparison with experiments

The numerical outcomes of the proposed model will be now compared with some of the experimental results reported in the paper by Lloyd (1994). The mechanical tests considered therein were obtained on particle reinforced light metal composites made up of an A365 aluminum alloy matrix and SiC reinforcing particles. The composite material was fabricated with 15% volume fraction of reinforcing particles. The particle size induced strengthening was evaluated by comparing the mechanical response for different sizes of the reinforcement, i.e. 7.5 μm and 16 μm. To fit the typical strain hardening of the A365 aluminum matrix, the function $\mathcal{H}\left(\epsilon_0^p\right)$ was selected as a modified Voce function as follows

$$\mathcal{H}\left(\epsilon_0^p\right) = \frac{1}{\sigma_{ref}}\left\{\sigma_Y + \kappa\,\epsilon_0^p + R_\infty\left(1 - \exp\left[-m\,\epsilon_0^p\right]\right)\right\}, \tag{34}$$

where $\sigma_Y = 105$ MPa, $\kappa = 600$ MPa, $R_\infty = 90$ MPa, and $m = 150$ are hardening parameters, while $\sigma_{ref} = 250$ MPa is taken as the reference stress.

Fig. 12a shows the comparison between the considered experimental results and the outcomes of the numerical analyses assuming the matrix undamageable. This particular condition served as a reference case to adjust the parameters of the SGP model according to the experimental curves for moderate applied strain, i.e. in the regime where the impact of damage is supposed to be negligible. In particular, it turned out that the size dependent strain hardening of the composite is well captured for $\ell_p = 40$ μm in the strain regime $E_{11} < 0.05$. On the contrary, for a higher magnitude of the applied macroscopic strain, the numerical simulations clearly overestimate the composite stress as no damage mechanisms has been included.

Damage evolution was then activated in the subsequent simulations in order to evaluate the numerical results of the complete extended non-local model. In this case, the numerical analyses were parametrized with respect to the parameters f_N and ℓ_d while the other material constants of the extended GTN model were selected as in Section 4.1. A first set of numerical results, not reported here for the sake of brevity, showed a negligible impact of parameter ℓ_d (taken in the range $0.1 \div 5$ μm) for the considered magnitude of the applied strain. On the other hand, parameter f_N affects significantly the magnitude of the simulated macroscopic stress as reported in Fig. 12b. In particular, the comparison between Fig. 12a and 12b remarks a significant reduction of the composite stress for the damageable matrix in the regime $E_{11} > 0.05$. In the case of $f_N = 0.04$, the experimental results for the 16 μm particle size composite are well captured in the whole strain range while the curves of the 7.5 μm composite are overestimated. A different scenario is obtained for $f_N = 0.08$ in which the numerical analyses slightly overestimate and underestimate the composite stress for 7.5 μm and 16 μm reinforcement size, respectively.

5. Summary and conclusions

In this paper we analyze the reinforcement size effect in a particle reinforced composite by means of computational homogenization along with the use of non-local versions of plasticity and ductile damage. To this end, the lower-order SGP model of Huang et al. (2004) and the implicit gradient regularization of damage for multi-phase media (Magri et al., 2021) are employed to enhance the classical GTN model. As a result of that, two length scale parameters are introduced in the extended model, one for each non-local extension, which modulate the size sensitivity of the problem. The resulting formulation consists of a coupled system of three partial differential equations (i.e. the classical balance of linear momentum and the two Helmholtz-type equations of the damage regularization) which are solved via the FFT-based algorithm proposed in Magri et al. (2021). The latter exploits an iterative staggered scheme that incorporates an FFT-Galerkin solver for the solution of the purely mechanical problem, and a conjugate gradient spectral solver for the Helmholtz-type equations.

A series of numerical simulations are performed on three-dimensional microstructures of particle reinforced metal matrix composites. The impact of each non-local extension of the GTN model is first analyzed separately as a function of each relevant length parameter. The obtained numerical results show that the SGP model induces a particle size dependent strengthening in the composite, resulting in a stronger response for smaller particles. This reproduces the experimental trends shown in most studies. In addition, the non-local regularization of the damage affects the ductility of the homogenized response inducing a higher ductility for a smaller size of the reinforcements. The latter result can be explained by the fact that microvoid damage is the only degradating mechanism considered in this numerical study. This experimental trend has been observed only for high temperatures (Lloyd, 1994), where it is expected that the particle debonding is hindered by the low yield stress and, as in this model, ductile damage in the matrix is the only relevant damage mechanism. The combined effect of the considered non-local models is also investigated by studying the change in the resulting strengthening and ductility as a function of the particle size of the composite. Finally, a comparative study with experimental results confirms that the particle size induce strengthening in metal matrix composites can be quantitatively captured by the considered model.

Future developments will focus on adding alternative damaging mechanisms in the composite material within this non-local setting, e.g. particle–matrix debonding and particle fracturing. It is, indeed, well known that the mechanical response of metal matrix composites results from the competition of multiple degradation mechanisms acting on different length scales. These improvements will potentially allow us to get more insights on the physical nature of the length parameters involved with non-local models through a more reliable comparison with experimental results.

CRediT authorship contribution statement

M. Magri: Conceptualization, Methodology, Software, writing – original draft. **L. Adam:** Funding acquisition. **J. Segurado:** Conceptualization, Methodology, Funding acquisition, writing – review & editing.

Declaration of competing interest

The authors declare that they have no known competing financial interests or personal relationships that could have appeared to influence the work reported in this paper.

Acknowledgment

The authors gratefully acknowledge the support provided by the Luxembourg National Research Fund (FNR), Reference No. 12737941. JS and MM also acknowledge the European Union's Horizon 2020 research and innovation programme for the project "Multi-scale Optimization for Additive Manufacturing of fatigue resistant shock-absorbing MetaMaterials (MOAMMM)", grant agreement No. 862015, of the H2020-EU.1.2.1. - FET Open Programme.

Appendix A. FFT-Galerkin solver

The solution of equation ((21)a) is calculated using the Galerkin FFT method of Vondřejc et al. (2014) and Zeman et al. (2017) together with the procedure to incorporate stress and mixed control proposed by Lucarini and Segurado in Lucarini and Segurado (2019a). Such a control technique sets a combination of components of the macroscopic strain (h, k) and/or the macroscopic stress (H, K) history, i.e. $E_{hk}(t)$ and $\Sigma_{HK}(t)$, respectively. The boundary value problem is then solved expressing the weak form of the linear momentum balance for the current time increment

$$\begin{cases} \int_{\Omega} \mathbb{G}^* * \boldsymbol{\zeta}(\vec{x}) : \boldsymbol{\sigma}\left(\boldsymbol{\varepsilon}(\vec{x}), \vec{\alpha}\right) \mathrm{d}V & = 0\,, \\ \langle \sigma \rangle_{HK} & = \Sigma_{HK}\big|_{n+1}\,, \\ \langle \varepsilon \rangle_{hk} & = E_{hk}\big|_{n+1}\,, \end{cases} \tag{35}$$

where $\langle \cdot \rangle$ represents the volume average, $\mathbb{G}^*$ stands for the projector operator that enforces the compatibility of the test functions, $\boldsymbol{\zeta}(\vec{x})$ are second order tensor test functions, $*$ is the convolution operation, and the indices of the macroscopic stress and strain obey $i, j \cap I, J = \emptyset$. In (35) the original projection operator for small strain proposed in de Geus et al. (2017) is replaced by a modified $\mathbb{G}^*$ that includes modified zero frequencies to enforce the value of stress averages and has a closed-form expression in Fourier space $\widehat{\mathbb{G}^*}$ (Lucarini and Segurado, 2019a). Moreover, in order to reduce numerical noise, the modified frequencies Eq. (26) resulting from the use of the discrete derivation rule presented in Section 3.3 are used for the definition of this operator.

After performing the spatial discretization described in Section 3.3, the weak form of the equilibrium Eq. (35) results in an algebraic system of non-linear equations (Vondřejc et al., 2014)

$$\mathcal{G}^*(\boldsymbol{\sigma}) := \mathcal{F}^{-1}\left\{\widehat{\mathbb{G}}^* : \mathcal{F}\left(\boldsymbol{\sigma}\left(\boldsymbol{\varepsilon}(\vec{x}), \vec{\alpha}\right)\right)\right\} = \mathbf{0}\,, \tag{36}$$

with symbol $\mathcal{F}$ indicating the Fourier transform. A Newton–Raphson algorithm is adopted for the solution of the resulting non-linear problem so that the stress tensor is linearized with respect to the total strain as

$$\boldsymbol{\sigma}^{(r+1)} = \boldsymbol{\sigma}^{(r)} + \frac{\partial \boldsymbol{\sigma}}{\partial \boldsymbol{\varepsilon}} : \delta\boldsymbol{\varepsilon}^{(r+1)}\,. \tag{37}$$

where $\delta\boldsymbol{\epsilon}^{(r+1)}$ is the strain correction for Newton–Raphson iteration $r+1$. A linear problem is finally obtained by substitution of (37) into (36)

$$\mathcal{G}^*\left(\frac{\partial\boldsymbol{\sigma}}{\partial\boldsymbol{\epsilon}} : \delta\boldsymbol{\epsilon}^{(r+1)}\right) = -\mathcal{G}^*\left(\boldsymbol{\sigma}^{(r)} - \overline{\boldsymbol{\Sigma}}_{n+1}\right),$$

where $\overline{\boldsymbol{\Sigma}}\Big|_{n+1}$ is a tensor containing the non-zero HK components of the imposed stress at time t_{n+1}. Such a linear problem is solved using the conjugate gradient method, whose convergence rate, efficiency, and memory allocation are optimal for this problem.

Appendix B. FFT solver for the Helmholtz-type equations

The Helmholtz-type equations ((21)a–c) can be rewritten in abstract setting as

$$\overline{\alpha} - \operatorname{div}\left[\ell_d^2(\vec{x})\,\nabla\overline{\alpha}\right] = \alpha,$$

where α is a generic local variable while $\bar{\alpha}$ is the non-local counterpart of α. This problem can be rephrased in a more convenient form as

$$\text{Find } \overline{\alpha} \text{ such that } \mathcal{L}\left(\overline{\alpha}\right) = \alpha, \tag{38}$$

where $\mathcal{L} = (\bullet) - \operatorname{div}\left[\ell_d^2(\vec{x})\,\nabla(\bullet)\right]$ is a linear differential operator. In spectral solvers, problem (38) can be easily solved in the frequency domain because it reduces to the following linear problem

$$\mathcal{F}\left(\mathcal{L}\left(\overline{\alpha}\right)\right) = \mathcal{F}\left(\alpha\right) \tag{39}$$

where symbol $\mathcal{F}$ indicates the Fourier transform operator. The derivation of the left-hand side of Eq. (39) is straightforward in Fourier space and holds

$$\mathcal{F}\left(\mathcal{L}\left(\overline{\alpha}\right)\right) = \mathcal{F}\left(\overline{\alpha}\right) + \vec{\xi}\cdot\mathcal{F}\left(\ell_d^2(\vec{x})\,\mathcal{F}^{-1}\left(\vec{\xi}\mathcal{F}\left(\overline{\alpha}\right)\right)\right),$$

where $\vec{\xi}$ is the frequency vector. Therefore, the linear problem (39) rewrites in Fourier space as

$$\widehat{\mathcal{L}}\left(\mathcal{F}\left(\overline{\alpha}\right)\right) = \mathcal{F}\left(\alpha\right),$$

with

$$\widehat{\mathcal{L}} = (\bullet) + \vec{\xi}\cdot\mathcal{F}\left(\ell_d^2(\vec{x})\,\mathcal{F}^{-1}\left(\vec{\xi}\ (\bullet)\right)\right).$$

Such an equation is solved numerically exploiting a conjugate gradient algorithm. Following the approach proposed in Lucarini and Segurado (2019b) for a displacement based FFT homogenization algorithm the usage of the following preconditioner

$$\mathcal{M}\left(\mathcal{F}\left(\overline{\alpha}\right)\right) = \left[1 + \frac{\ell_d^M + \ell_d^S}{2}\,\vec{\xi}\cdot\vec{\xi}\right]^{-1}\mathcal{F}\left(\overline{\alpha}\right)$$

speeds up significantly this iterative algorithm.

Appendix C. Objective calculation of plastic strain gradients

The purpose of this section is to justify the need of an objective numerical derivative for the implementation of SGP models in spectral solvers and show how the approach proposed is able to provide discretization independent results for the gradient term.

In the case of heterogeneous media, where different material phases constitute the material microstructure, some of the field variables of the problem might be discontinuous at the phase interfaces. If the constitutive theory depends on the spatial derivative of such fields, as it happens in strain gradient plasticity, the numerical solutions through FFT-solvers might lead to numerical noise or to a spurious grid dependence depending on how the derivative is performed numerically. For instance, it is well known that the derivative of a step-like function φ (see Fig. 13) using the standard derivative in discrete Fourier space leads to numerical noise. In order to alleviate this problem, discrete differences discrete derivative rules are used instead. The result is the elimination of the noise, but paying the prize of introducing a prominent grid dependence, as it can be observed in Fig. 14a when the discrete derivative in Eq. (26) is applied to the step-like function φ. Therefore, this numerical derivative cannot be regarded as an objective operator. As discussed in Section 3.4, one possible strategy for alleviating this grid dependence is to apply the implicit gradient regularization Eq. (28) to the original non-objective derivative. Fig. 14b supports this choice since the proposed alternative operator produces converging results for a decreasing grid size. It is worth recalling that the magnitude of this objective derivative depends on the length-parameter ℓ_ε. In particular, the higher the constant ℓ_ε, the lower the magnitude of the derivative.

In order to prove that the proposed objective derivative produces grid independent results, a convergence study for the considered MSGP model is reported here. This study is carried out by simulating the homogenized mechanical response of a selected RVE topology with different digital resolutions. The reference RVE is generated with a low digital resolution, i.e. with 32^3 voxels, and then discretized also with 64^3 and 96^3 voxels in a way such that the RVE topology is conserved (for instance compare the shape of the reinforcements for the three different resolutions in Fig. 17). The simulations are then performed by accounting for the

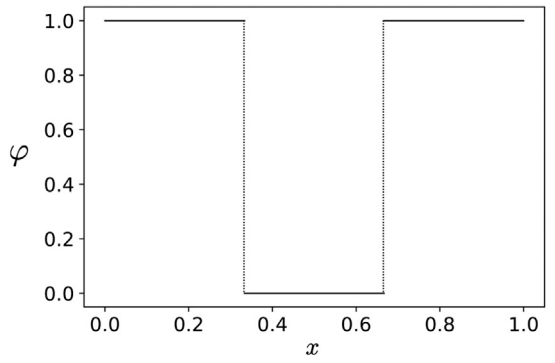

Fig. 13. Plot of the step function φ used for comparing the considered numerical derivatives.

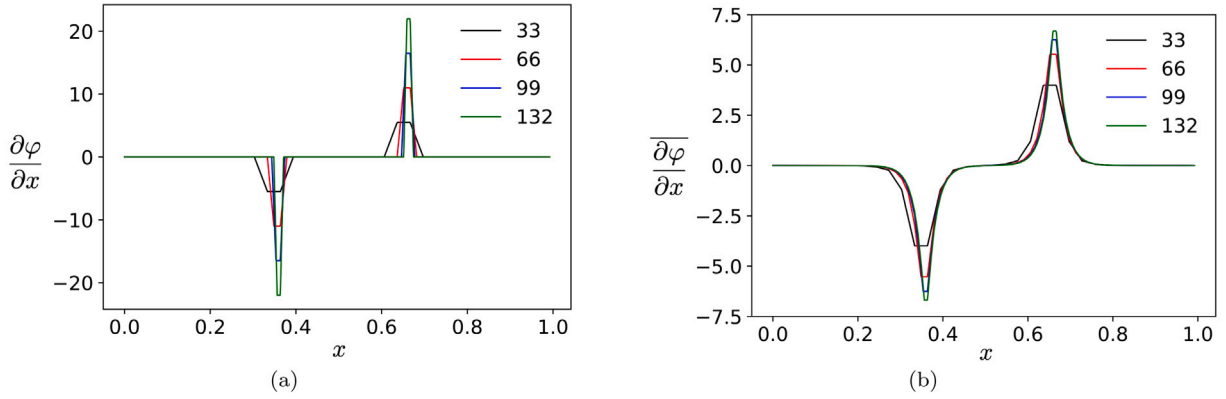

Fig. 14. Comparison between the spatial derivative obtained (a) by application of the original discrete differential operator Eq. (26) and (b) by using the objective discrete derivative Eq. (28). For both graphs are reported the results obtained with different digital resolutions along the x axis, i.e. 33, 66, 99, 132 voxels. The length-parameter used to generate the results reported in (b) is selected as $\ell_\varepsilon = 2/33$ for each grid discretization.

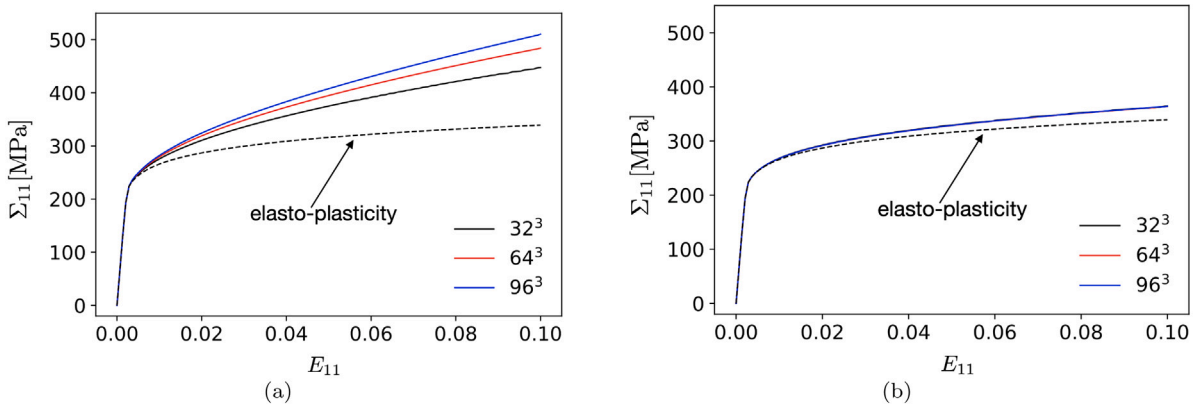

Fig. 15. Comparison between the numerical predictions of the considered SGP model for different RVE resolutions in the case of η^p defined (a) by the original discrete derivative Eq. (27) and (b) by the objective one proposed here (see Eq. (29)). The simulations were carried out by taking $\ell_p^* = 2$ and $\ell_\varepsilon = 2/32L$. The dashed curve represents the reference, grid independent, case in which strain gradient effects are suppressed by assigning $\ell_p^* = 0$.

considered MSGP model as conducted in Section 4.2.1. Fig. 15 plots the homogenized response for the different grid resolutions in the case where η^p is computed via (i) the original discrete derivative (see Fig. 15a) and (ii) using the proposed objective derivative (see Fig. 15b). The comparison between these two cases clearly shows that the proposed alternative derivative rule provides grid independent results. Moreover, due to the smoothening operated by Eq. (28) on the components of the plastic strain gradient, the strengthening induced by the MSGP is smaller than the one obtained using the original discrete derivative. This last result arises because parameter ℓ_ε is somehow large, compared to the RVE size, since it is selected based on the coarsest grid resolution.

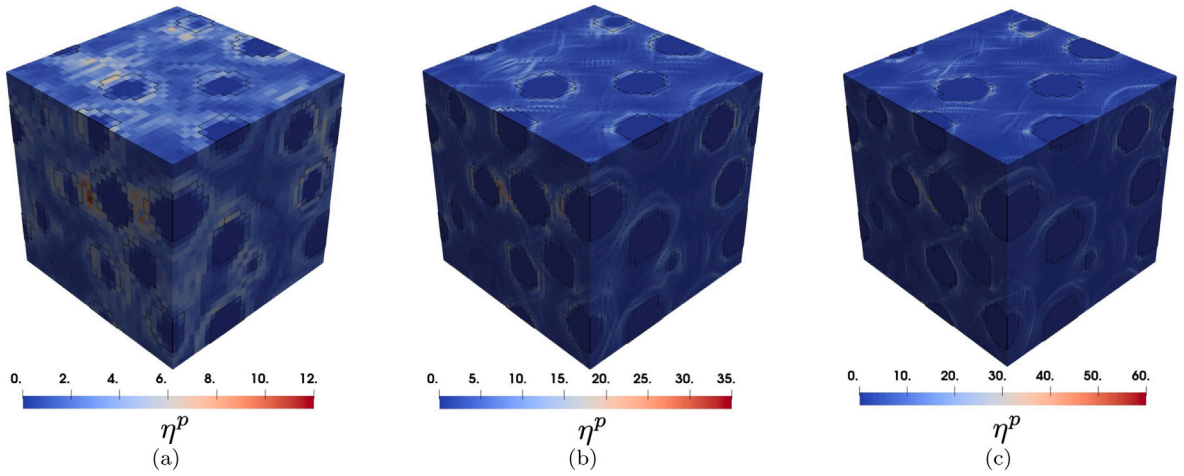

Fig. 16. Spatial distribution of the equivalent plastic strain gradient η^p at the end of the simulation obtained using the original discrete differential operator Eq. (27). The results are reported for different RVE resolutions, i.e. (a) 32^3, (b) 64^3, and (c) 96^3 voxels. For each image, the black line draws the particle/matrix interface.

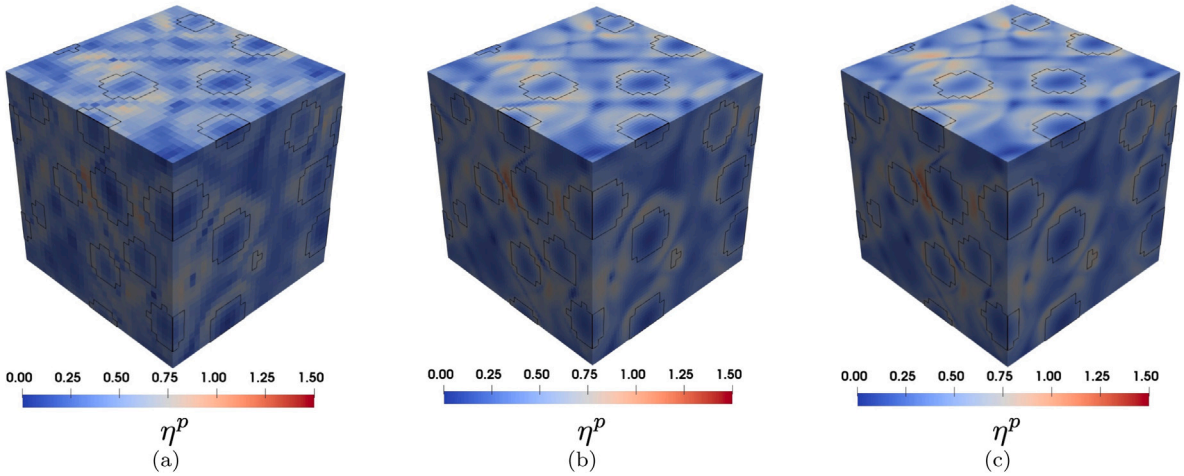

Fig. 17. Spatial distribution of the equivalent plastic strain gradient η^p at the end of the simulation obtained using the proposed objective numerical derivative Eq. (29). The results are reported for different RVE digital, i.e. (a) 32^3, (b) 64^3, and (c) 96^3 voxels. For each image, the black line draws the particle/matrix interface.

Figs. 16 and 17 report the spatial distribution of η^p at the end of each simulation for the different derivative operators. If the original discrete derivative is considered, the distribution of η^p is remarkably different for the considered grid resolutions. Moreover, the relevant plots show a sort of strain gradient localization far from the reinforcing particles that does not seems to have a clear physical background. On the other hand, a grid independent distribution of η^p is obtained if the proposed objective derivative is employed. In this case, the regularization operated by Eq. (28) effectively suppresses spurious strain gradient localizations far from the reinforcing particles providing a more physical distribution of η^p.

References

Aifantis, E.C., 1987. The physics of plastic deformation. Int. J. Plast. 3 (3), 211–247.
Arsenlis, A., Parks, D.M., 1999. Crystallographic aspects of geometrically-necessary and statistically-stored dislocation density. Acta Mater. 47 (5), 1597–1611.
Ashby, M.F., 1970. The deformation of plastically non-homogeneous materials. Phil. Mag. 21 (170), 399–424.
Babout, L., Maire, E., Buffière, J.Y., Fougères, R., 2001. Characterization by X-ray computed tomography of decohesion, porosity growth and coalescence in model metal matrix composites. Acta Mater. 49 (11), 2055–2063.
Babout, L., Maire, E., Fougères, R., 2004. Damage initiation in model metallic materials: X-ray tomography and modelling. Acta Mater. 52 (8), 2475–2487.
Ban, H., Peng, Z., Fang, D., Yao, Y., Chen, S., 2020. A modified conventional theory of mechanism-based strain gradient plasticity considering both size and damage effects. Int. J. Solids Struct. 202, 384–397.

Bassani, J.L., 2001. Incompatibility and a simple gradient theory of plasticity. J. Mech. Phys. Solids 49 (9), 1983–1996, The JW Hutchinson and JR Rice 60th Anniversary Issue.
Bassani, J.L., Needleman, A., Van der Giessen, E., 2001. Plastic flow in a composite: a comparison of nonlocal continuum and discrete dislocation predictions. Int. J. Solids Struct. 38 (5), 833–853.
Berbenni, S., Taupin, V., Djaka, K.S., Fressengeas, C., 2014. A numerical spectral approach for solving elasto-static field dislocation and g-disclination mechanics. Int. J. Solids Struct. 51 (23), 4157–4175.
Boeff, M., Gutknecht, F., Engels, P.S., Ma, A., Hartmaier, A., 2015. Formulation of nonlocal damage models based on spectral methods for application to complex microstructures. Eng. Fract. Mech. 147, 373–387.
Böhm, H.J., Han, W., Eckschlager, A., 2004. Multi-inclusion unit cell studies of reinforcement stresses and particle failure in discontinuously reinforced ductile matrix composites. Comput. Model. Eng. Sci. 5 (1), 5–20.
Brenner, R., Beaudoin, A.J., Suquet, P., Acharya, A., 2014. Numerical implementation of static field dislocation mechanics theory for periodic media. Phil. Mag. 94 (16), 1764–1787.
Chu, C.C., Needleman, A., 1980. Void nucleation effects in biaxially stretched sheets. Trans. ASME, J. Eng. Mater. Technol. 102 (3), 249–256.
Dai, L.H., Ling, Z., Y.L., Bai., 2001. Size-dependent inelastic behavior of particle-reinforced metal–matrix composites. Compos. Sci. Technol. 61 (8), 1057–1063.
Dorhmi, K., Morin, L., Derrien, K., Hadjem-Hamouche, Z., Chevalier, J.P., 2020. A homogenization-based damage model for stiffness loss in ductile metal-matrix composites. J. Mech. Phys. Solids 137, 103812.
Drabek, T., Böhm, H.J., 2005. Damage models for studying ductile matrix failure in composites. Comput. Mater. Sci. 32 (3), 329–336, IWCMM.
Drabek, T., Böhm, H.J., 2006. Micromechanical finite element analysis of metal matrix composites using nonlocal ductile failure models. Comput. Mater. Sci. 37 (1), 29–36, Proceedings of the 14th International Workshop on Computational Mechanics of Materials.
Eringen, A.C., 1966. A unified theory of thermomechanical materials. Int. J. Eng. Sci. 4 (2), 179–202.
Fleck, N.A., Hutchinson, J.W., 2001. A reformulation of strain gradient plasticity. J. Mech. Phys. Solids 49 (10), 2245–2271.
Fleck, N.A., Muller, G.M., Ashby, M.F., Hutchinson, J.W., 1994. Strain gradient plasticity: Theory and experiment. Acta Mater. 42 (2), 475–487.
Gao, H., Huang, Y., Nix, W.D., Hutchinson, J.W., 1999. Mechanism-based strain gradient plasticity — I. Theory. J. Mech. Phys. Solids 47 (6), 1239–1263.
de Geus, T.W.J., Vondřejc, J., Zeman, J., Peerlings, R.H.J., Geers, M.G.D., 2017. Finite strain FFT-based non-linear solvers made simple. Comput. Methods Appl. Mech. Engrg. 318, 412–430.
Gudmundson, P., 2004. A unified treatment of strain gradient plasticity. J. Mech. Phys. Solids 52 (6), 1379–1406.
Gurson, A.L., 1977. Continuum theory of ductile rupture by void nucleation and growth: Part I—Yield criteria and flow rules for porous ductile media. Trans. ASME, J. Eng. Mater. Technol. 99 (1), 2–15.
Gurtin, M.E., Anand, L., 2005. A theory of strain-gradient plasticity for isotropic, plastically irrotational materials. Part I: Small deformations. J. Mech. Phys. Solids 53 (7), 1624–1649.
Gustafson, T.W., Panda, P.C., Song, G., Raj, R., 1997. Influence of microstructural scale on plastic flow behavior of metal matrix composites. Acta Mater. 45 (4), 1633–1643.
Haouala, S., Lucarini, S., LLorca, J., Segurado, J., 2020. Simulation of the hall-petch effect in FCC polycrystals by means of strain gradient crystal plasticity and FFT homogenization. J. Mech. Phys. Solids 134, 103755.
Huang, Y., Gao, H., Nix, W.D., J.W., Hutchinson., 2000. Mechanism-based strain gradient plasticity — II. Analysis. J. Mech. Phys. Solids 48 (1), 99–128.
Huang, Y., Qu, S., Hwang, K.C., Li, M., Gao, H., 2004. A conventional theory of mechanism-based strain gradient plasticity. Int. J. Plast. 20 (4), 753–782.
Huber, G., Brechet, Y., T., Pardoen, 2005. Predictive model for void nucleation and void growth controlled ductility in quasi-eutectic cast aluminium alloys. Acta Mater. 53 (9), 2739–2749.
Ibrahim, I.A., Mohamed, F.A., Lavernia, E.J., 1991. Particulate reinforced metal matrix composites – a review. J. Mater. Sci. 26, 1137–1156.
Jirasek, M, 2007. Modeling Of Localized Inelastic Deformation. Czech Technical University.
Lebensohn, R.A., Needleman, A., 2016. Numerical implementation of non-local polycrystal plasticity using fast Fourier transforms. J. Mech. Phys. Solids 97, 333–351, SI:Pierre Suquet Symposium.
Lemaitre, J., 1985. A continuous damage mechanics model for ductile fracture. Trans. ASME, J. Eng. Mater. Technol. 107 (1), 83–89.
Liu, B., Huang, W.M., Wang, H.W., Wang, M.L., Li, X.F., 2014. Study on the load partition behaviors of high particle content B4C/Al composites in compression. J. Compos. Mater. 48 (3), 355–364.
LLorca, J., Segurado, J., 2004. Three-dimensional multiparticle cell simulations of deformation and damage in sphere-reinforced composites. Mater. Sci. Eng. A 365 (1), 267–274.
Lloyd, D.J., 1994. Particle reinforced aluminium and magnesium matrix composites. Int. Mater. Rev. 39 (1), 1–23.
Lucarini, S., Segurado, J., 2019a. An algorithm for stress and mixed control in Galerkin-based FFT homogenization. Int. J. Numer. Methods Eng. 119 (8), 797–805.
Lucarini, S., Segurado, J., 2019b. DBFFT: A displacement based FFT approach for non-linear homogenization of the mechanical behavior. Int. J. Eng. Sci. 144, 103131.
Lucarini, S., Segurado, J., 2019c. On the accuracy of spectral solvers for micromechanics based fatigue modeling. Comput. Mech. 63, 365–382.
Magri, M., Lucarini, S., Lemoine, G., Adam, L., Segurado, J., 2021. An FFT framework for simulating non-local ductile failure in heterogeneous materials. Comput. Methods Appl. Mech. Eng. 380, 113759.
Marano, A., Gélébart, L., S., Forest, 2019. Intragranular localization induced by softening crystal plasticity: Analysis of slip and kink bands localization modes from high resolution FFT-simulations results. Acta Mater. 175, 262–275.
Matouš, K., Geers, M.G.D., Kouznetsova, V.G., Gillman, A., 2017. A review of predictive nonlinear theories for multiscale modeling of heterogeneous materials. J. Comput. Phys. 330, 192–220.
Miehe, C., Schaenzel, L.M., Ulmer, H., 2015. Phase field modeling of fracture in multi-physics problems. Part I. Balance of crack surface and failure criteria for brittle crack propagation in thermo-elastic solids. Comput. Methods Appl. Mech. Engrg. 294, 449–485.
Milan, M.T., Bowen, P., 2004. Ensile and fracture toughness properties of SiCp reinforced al alloys: Effects of particle size, particle volume fraction, and matrix strength. J. Mater. Eng. Perform. 13, 775–783.
Moulinec, H., Suquet, P., 1994. A fast numerical method for computing the linear and nonlinear mechanical properties of composites. C. R. Acad. Sci. Ser. II.
Moulinec, H., Suquet, P., 1998. A numerical method for computing the overall response of nonlinear composites with complex microstructure. Comput. Methods Appl. Mech. Engrg. 157 (1), 69–94.
Nguyen, V.D., Pardoen, T., Noels, L., 2020. A nonlocal approach of ductile failure incorporating void growth, internal necking, and shear dominated coalescence mechanisms. J. Mech. Phys. Solids 137, 103891.
Nix, W.D., Gao, H., 1998. Indentation size effects in crystalline materials: A law for strain gradient plasticity. J. Mech. Phys. Solids 46 (3), 411–425.
Nye, J.F., 1953. Some geometrical relations in dislocated crystals. Acta Metall. 1 (2), 153–162.
Peerlings, R.H.J., De Borst, R., Brekelmans, W.A.M., De Vree, J.H.P., 1996. Gradient enhanced damage for quasi-brittle materials. Int. J. Numer. Methods Eng. 39 (19), 3391–3403.
Reusch, F., Hortig, C., Svendsen, B., 2008. Nonlocal modeling and simulation of ductile damage and failure in metal matrix composites. J. Eng. Mater. Technol. 130 (2), 021009.
Segurado, J., Llorca, J., 2002. A numerical approximation to the elastic properties of sphere-reinforced composites. J. Mech. Phys. Solids 50 (10), 2107–2121.

Segurado, J., LLorca, J., 2005. A computational micromechanics study of the effect of interface decohesion on the mechanical behavior of composites. Acta Mater. 53 (18), 4931–4942.
Shakoor, M., Bernacki, M., Bouchard, P.O., 2018. Ductile fracture of a metal matrix composite studied using 3D numerical modeling of void nucleation and coalescence. Eng. Fract. Mech. 189, 110–132.
Simo, J.C., Hughes, T., 2006. Computational Inelasticity. vol. 7, Springer Science & Business Media.
Steinke, C., Zreid, I., Kaliske, M., 2017. On the relation between phase-field crack approximation and gradient damage modelling. Comput. Mech. 59, 717–735.
Taylor, G.I., 1934. The mechanism of plastic deformation of crystals. Part I. – Theoretical. Proc. R. Soc. Lond. Ser. A 145, 362–387.
Taylor, G.I., 1938. Plastic strain in metals. J. Inst. Met. 62, 307–324.
Tvergaard, V., Needleman, A., 1984. Analysis of the cup-cone fracture in a round tensile bar. Acta Metall. 32 (1), 157–169.
Vondřejc, J., Zeman, J., Marek, I., 2014. An FFT-based Galerkin method for homogenization of periodic media. Comput. Math. Appl. 68 (3), 156–173.
Voyiadjis, G.Z., Song, Y., 2019. Strain gradient continuum plasticity theories: Theoretical, numerical and experimental investigations. Int. J. Plast. 121, 21–75.
Weck, A., Wilkinson, D.S., Maire, E., 2008. Observation of void nucleation, growth and coalescence in a model metal matrix composite using X-ray tomography. Mater. Sci. Eng. A 488 (1), 435–445.
Weng, L., Fan, T., Wen, M., Shen, Y, 2019. Three-dimensional multi-particle FE model and effects of interface damage, particle size and morphology on tensile behavior of particle reinforced composites. Compos. Struct. 209, 590–605.
Willot, F., 2015. Fourier-based schemes for computing the mechanical response of composites with accurate local fields. C. R. Méc. 343 (3), 232–245.
Yan, Y.W., Geng, L., Li, A.B., 2007. Experimental and numerical studies of the effect of particle size on the deformation behavior of the metal matrix composites. Mater. Sci. Eng. A 448 (1), 315–325.
Zeman, J., de Geus, T.W.J., Vondrejc, J., Peerlings, R.H.J., Geers, M.G.D., 2017. A finite element perspective on nonlinear FFT-based micromechanical simulations. Int. J. Numer. Methods Eng. 111 (10), 903–926.
Zhang, J.F., Andrä, H., Zhang, X.X., Wang, Q.Z., Xiao, B.L., Ma, Z.Y., 2019. An enhanced finite element model considering multi strengthening and damage mechanisms in particle reinforced metal matrix composites. Compos. Struct. 226, 111281.
Zhou, L., Li, S., Huang, S., 2011. Simulation of effects of particle size and volume fraction on al alloy strength, elongation, and toughness by using strain gradient plasticity concept. Mater. Des. 32 (1), 353–360.